VIV-induced strain on a lazy wave dynamic marine power cable in a steady current

R. Moideen[a], V. Venugopal[a*], J.R. Chaplin[b] and A.G.L. Borthwick[a]

[a]*School of Engineering, The University of Edinburgh, UK*
[b]*Faculty of Engineering and the Environment, University of Southampton, UK*

Abstract

Marine power cables are commonly used to transfer electricity from offshore renewable energy (ORE) devices to shore. Such cables are susceptible to fatigue failure due to flow-induced vibration. We present results from physical model tests conducted at Edinburgh University's FloWave wave-current facility on an instrumented flexible cable in a lazy wave configuration subjected to a steady, unidirectional current. The Reynolds number was subcritical, ranging from 3,100 to 24,800. Bending strain was measured at seven locations along the length of the cable and the results are presented in terms of cable curvature. The data analysis shows that, currents propagating normal to the longitudinal axis of the cable caused large local variations in curvature. The maximum variation in curvature occurred near the touchdown zone and at the sag bend. Repeated high-amplitude cyclic loading was observed in currents directed at angles within ± 30^o normal to the longitudinal axis of the cable. Significant shifts in peak frequency and spectral energy distribution were evident with increasing reduced velocity. At certain locations along the cable, the strain frequency corresponded to a Strouhal number of 0.127 - 0.144, whereas very low peak strain frequencies occurred elsewhere. The strain behaviour was sensitive to the current speed and direction relative to the orientation of the cable. Mono-frequency strain responses occurred at lower reduced velocity and multi-frequency responses at higher reduced velocity.

Keywords: Vortex induced vibration (VIV), Offshore power cable, Lazy wave configuration, Strouhal number, Bending strain, offshore renewable energy

Highlights

- Currents perpendicular to the longitudinal axis of a marine cable cause significant local variation in curvature, especially near the touchdown zone and sag bend.
- Strain response is broader band at higher current speed.
- Strouhal number ranges between 0.13 and 0.14, with no clear lock-in behaviour observed in these tests.
- We believe this is the first comprehensive experimental study of a marine power cable in a lazy wave configuration.

1. Introduction

Slender marine power cables are commonly used to transfer electricity from offshore renewable energy (ORE) devices to onshore substations. Being immersed in the sea, such power cables experience forces due to currents, waves, turbulence, and the motion of floating ORE structures. Vortex-induced vibration (VIV) poses a major challenge to the survivability of marine power cables which are critical components of offshore renewable energy systems. In most of the ORE structures, the lazy wave configuration is preferred to catenary or straight cables for several reasons: superior performance in reducing maximum tension and lowering fatigue damage; ease of installation; lower buoyancy requirements; and reduced subsea hardware. Consequently, the lazy wave cable is more cost-effective than the alternative configurations (Martinelli et al., 2010). In lazy wave cables, the buoyancy modules serve to decouple platform motions from the touchdown point, thereby reducing the risk of failure in the touchdown zone.

Historically, research into VIV of long flexible cylinders focused on top-tensioned members (see e.g., Govardhan & Williamson, 2006; Sarpkaya, 2004; Chaplin et al., 2005 and Huera-Huarte & Bearman, 2009). The effect of cable end conditions was examined for currents of different (uniform and shear) flow profiles. Particular attention has been given to the vortex-induced vibration of a flexibly mounted rigid cylinder immersed in a current oriented normal to the long axis of the cylinder. Laboratory tests have also been conducted on the VIV of inclined cylinders (Lie & Kaasen, 2006; Vandiver et al., 2009; Jain & Modarres-Sadeghi, 2013 and Xu et al., 2018). Furthermore, Assi et al. (2014) investigated the response of curved cylinders in concave and convex configurations and found that the curved cylinders experienced lower vibration frequencies than corresponding straight cylinders.

Morooka & Tsukada (2013) conducted model tests on a catenary riser of 8 mm diameter, whose bottom rested on the floor and top was connected to a fixed support. The Reynolds number ranged from 500 to 600, far below the prototype value of the order of 10^5. Similarly, Fan et al. (2015) tested a catenary cable of diameter 20 mm, using strain gauges to record bending strain at six locations at Reynolds numbers up to 1.6×10^4. In both the foregoing studies, the catenary riser was aligned such that it was concave towards the incoming current. Similarly, Chaplin & King (2018) presented measurements of the response of a high-curvature non-tensioned catenary cable of diameter 56mm in concave, convex, and inclined configurations. The model had low bending stiffness and was tested at Reynolds numbers up to 7×10^4. Chaplin & King observed that the Strouhal number for their catenary profiles ranged from 0.11 to 0.13, well below the value of 0.2 associated with a rigid cylinder.

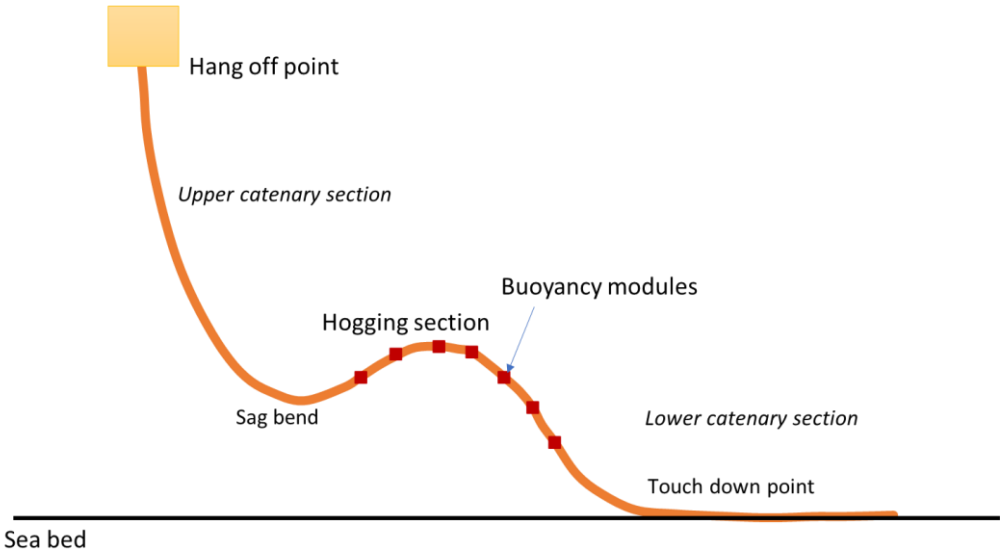

Figure1: Schematic of marine power cable in lazy wave configuration

Figure 1 illustrates an idealised lazy wave marine cable connected to the hang-off point of a floating ORE platform. Although Thies et al. (2012), Rentschler et al. (2019, 2020) and Yin (2022) numerically simulated the fluid-structure interaction of such a lazy wave cable, there is a shortage of high-quality laboratory data for validation purposes. This is particularly important because it has been established that significant differences occur in flow-induced vibrations experienced by catenary (Chaplin & King, 2018) and curved cylinders (Assi et al., 2014) . Our experimental tests address this research gap. However, as in other studies (e.g., Trim et al., 2005; Chaplin et al. 2005; Pereira et al., 2013; Morooka & Tsukada, 2013; Franzini et al., 2016 and Pesce et al., 2017) the test rig utilised in the present work involved a compromise because of constraints on the Reynolds number, cable geometry, structural properties, and measurement instrumentation due to limitations in the tank facility. For example, the Reynolds number at laboratory scale is one or two orders of magnitude lower than that at prototype scale, with repercussions for the vortex-induced vibrations. In a study of the VIV response of a spring-mounted rigid circular cylinder for $10^4 < Re < 10^6$, Raghavan & Bernitsas (2011) found that the vortex-induced vibration was particularly sensitive to the flow regime, with notable increases in response for Reynolds numbers in the range $4x10^4 < Re < 8x10^4$. From laboratory tests on long flexible cylinders of different diameters immersed in uniform and sheared currents, Resvanis et al. (2012) observed amplification of the lift coefficient and VIV response. They attributed this to the effect of Reynolds number which extended well into the critical flow regime ($Re = 5x10^3 < 2.2x10^5$). Within this Reynolds number range, the Strouhal number fell to between 0.13 and 0.14, unlike that for a rigid cylinder supported by springs (see Raghavan & Bernitsas, 2011) .

Our paper reports findings from systematic physical tests on a model marine power cable in a lazy wave configuration in a uniform steady current of varying speed and incident direction, following Moideen et al. (2024) . The model power cable was designed to preserve essential structural properties such as axial stiffness, bending stiffness, and mass ratio, the aim being to achieve reasonable dynamic similarity with a full-scale cable. The Reynolds number is in the range of 10^3 to 10^4. Our analysis of the flow-induced vibration of a lazy wave cable in a steady current should be useful in numerical model validation while contributing to a better understanding of the dynamic behaviour of power cables in the offshore environment. The paper is structured as follows. Section 2 describes the experimental setup, model design, and instrumentation. Section 3 presents and interprets the main results in terms of curvature time histories, spectra, and vibration frequencies, followed by a time-frequency analysis. Section 4 summarises the main findings.

2. Experimental set up

Physical tests on the model cable were conducted in the FloWave Ocean Energy Research Facility, located at the University of Edinburgh. FloWave is a 25 m diameter, 2 m deep circular basin in which regular and irregular, uni- and multi-directional waves over established ranges of frequencies and amplitudes can be produced using 168 computer-controlled active absorbing wave maker paddles. The facility can also generate currents up to 1.6 m/s in any horizontal direction by means of twenty-eight 1.7 m diameter impellers beneath the floor. The central part of the floor, 15 m in diameter, can be raised above the water surface for model installation. In the present study, uniform currents of speed ranging from 0.1 to 0.8 m/s were generated in seven different directions. A movable gantry located 1 m above still water level (SWL) provided supporting fixtures for rigidly attaching the model cable on to a load cell (data not reported here). A number of wave gauges (data not used in this paper) were fixed to this gantry. Figure 2 shows a plan view of the FloWave facility indicating the different current incident directions considered in the present study. The X, Y, Z axes have their origin at the centre of the tank floor. The X-axis is horizontal and aligned with the initial longitudinal axis of the cable extending from top to bottom. The Y-axis is transverse horizontal to the X-axis. Z is measured vertically upwards from the floor of the tank. Both ends of the model cable were located along the X-axis with the lower anchorage at X = 0.

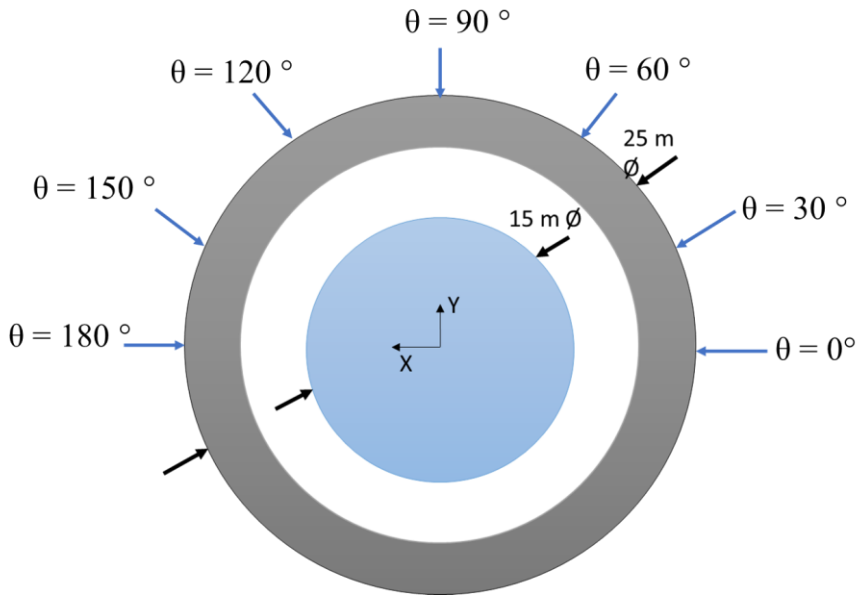

Figure 2: Plan view of the FloWave facility showing the test current directions.

2.1 Power cable model

The model cable was 5 m long and of 31 mm outer diameter. It is important to note that part of the cable was inserted into the top and bottom connections at the FloWave tank, which reduces the effective length to 4.93 m. It consisted of an inner core cable comprising a 3-core H07RN-F electric power cable of outer diameter 9.8 mm (Figure 3 (a)). This inner core cable was solely used to produce the required stiffness for the whole cable system and to provide a surface to attach strain gauges – it did not carry any electricity. Equidistant spacers, created through 3D printing (Figure 3 (b)), were evenly distributed over and along the length of the inner cable to provide housing for the strain gauge wires (Figures 3 (c) & (d)). As illustrated in Figure 3 (d), these spacers were 20 mm long and positioned at 20 mm intervals along the length of the cable. Each spacer had an outer diameter of 24 mm and a central opening of diameter 10.5 mm, designed to accommodate the core cable. The spacers were affixed onto the core cable using two small screws to prevent any movement. Strain gauges with pre-attached wiring systems (details provided in section 2.2) were affixed onto this inner cable at their outer surface, as shown in Figure 3 (c)), at seven prescribed locations, with full bridge connections employed to measure total bending strain at each location. Figure 3 (d) shows the system with strain gauges fixed; note that because the strain gauges were directly attached to the core cable, they are not visible due to the large number of wires used in the strain gauge connections at all stations. Finally, the entire 5 m inner cable assembly with spacers was inserted into the silicon tube, as depicted in Figure 3 (f). Table 1 lists details of the model cable including its material properties. The whole cable setup was filled with water during the tests to prevent kinks and to ensure the cable profile was uniform along its length.

Table 1: Cable properties

Scale model	
Length (m)	5 m (effective length is 4.93 m)
The total mass of cable	5.157 kg (excluding end connections is 4.526 kg)
Outside diameter (m)	0.031
Inner core cable	H07RN-F 3-core rubber cable
Inner core cable diameter (m)	9.8 mm
Inner core cable mass per unit length (g/m)	134 g/m
Mass ratio of cable	1.22
Submerged length of cable in water	4.16 m
Touchdown zone	1.35 m
Buoyancy section	1.12 m
Top section	2.279 m
Buoyancy modules	
Outside diameter	70 mm
Inside diameter	31 mm
Length	40 mm
Density	100 kg/m^3
No. of modules	5
3D printed bobbins	
Number of bobbins	118
Mass (g/piece)	4.4
Total mass	519.2 g
Silicon tube mass per m	250 g/m
Mass of strain gauges wires	461 g
Mass of water filled + dummy wires	1108.2 g

To create the Lazy wave profile, cylindrical buoyancy modules were fabricated from Divinycell of density 100 kg/m³. Table 1 lists their dimensions. The upper end of the cable was attached to a load cell, which was securely fixed to a 10 mm thick steel plate. This plate was then mounted to the gantry, while the lower end of the cable firmly fastened to the tank floor using the arrangement depicted in Figure 4 which shows the tank floor lifted above the water to facilitate the installation of the cable system.

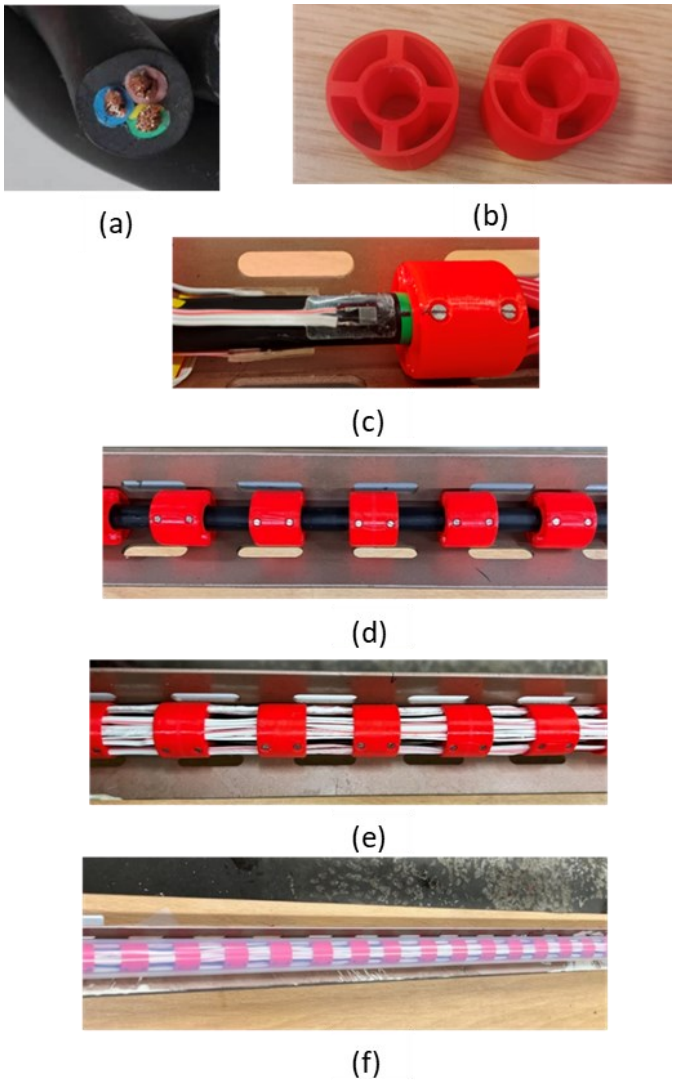

Figure 3: (a) Inner core cable; (b) 3D printed spacers; (c) strain gauge fixed to the cable; (d) spacer arrangement on the inner cable; (e) strain gauge wires arranged inside the spacers; and (f) model set-up inside the silicone tube.

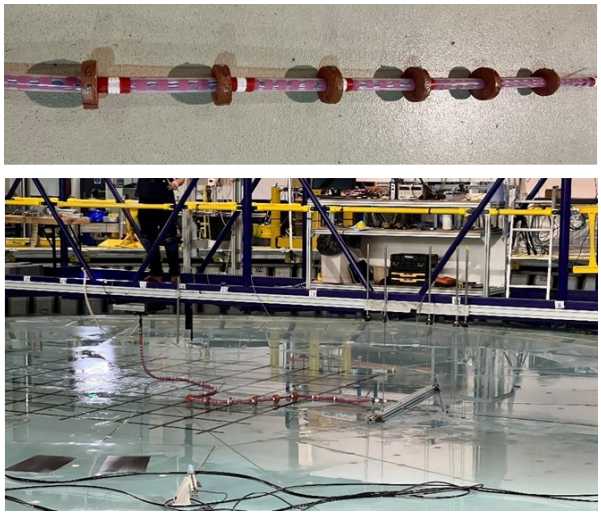

Figure 4: Cable with buoyancy modules (top) and its arrangement in the FloWave test facility (bottom). When the tank floor is lowered, the cable profile becomes a lazy wave.

2.2 Instrumentation

The 5 m cable was instrumented with 28 IP68 waterproof strain gauges (supplied by TechniMeasure, TML) at seven locations distributed along its length. At each location, four strain gauges positioned around the circumference of the inner core cable were configured in a full bridge to record the bending strain of the cable. The strain gauge cables emerged at the top of the model. To achieve uniform density, dummy lengths were included to ensure that at all points the cross section included the same number of cables. Labelled from the bottom as L1 to L7, the strain gauges were situated 0.5 m intervals apart. Each set of strain gauges utilized full bridge connections (see Appendix A) to measure total bending strain at a particular location regardless of current direction. The top end of the cable was connected to a 6-axis load cell fixed to the lowest elevation (0.7 m above still water level) of the gantry in air. The load cell measured forces and moments in X, Y and Z directions. Figure 5 shows the connection between the top of the cable and the load cell. The cable was also coated with stickers to capture displacements in X, Y and Z directions using a Qualisys motion tracking system. This paper primarily presents the strain gauge results; detailed results from the Qualisys sensors will be presented in a future paper. Selected findings from the additional displacement sensors are included herein to support the discussion of the strain gauge results. All data channels were sampled at 128 Hz with collection triggered at the onset of the current. This approach facilitated accurate, coordinated data acquisition at all specified locations.

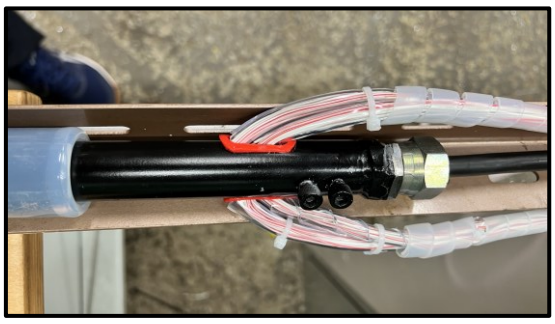

Figure 5: Cable top connection with the load cell, using a stiffener arrangement

2.3 Preliminary tests for estimating cable properties

For initial assessment of the structural properties of the cable, a 1 m sample was fabricated and instrumented. The sample was then subjected to preliminary tests to ascertain key characteristics including mass ratio and bending stiffness. The bending stiffness of the instrumented cable model and its inner core was measured using the TecQuipment SM1004 Beam Apparatus at the University of Exeter. At larger scale the model cable underwent testing to estimate its natural frequency and damping in air. The cable, suspended in a sagging position, was subjected to a free displacement decay test. A similar free displacement

response test was conducted under water for the lazy wave profile. Response frequencies were determined by applying a Fast Fourier Transform (FFT) to the recorded load time series of the cable, and the logarithmic decrement method used to calculate the damping ratio. Multiple iterations of these tests were conducted to check for repeatability, resulting in a comprehensive characterization of the natural frequency and damping ratio of the cable in air. Figure 6 shows the force time history of the cable undergoing damped free oscillations in air. Table 2 presents the structural properties, which have been scaled to replicate those of a prototype marine power cable. A scaling factor of 1:50 was adopted for the study, except for the cable diameter. All other structural parameters and input current conditions adhere to Froude scaling. The experiments were conducted at 1:50 scale, with current speeds varying from 0.1 to 0.9 m/s, corresponding to full-scale current speeds of 0.707 to 6.36 m/s. This range is consistent with real-world tidal currents observed at sites of the European Marine Energy Test Centre (https://www.emec.org.uk/) in the Orkney and Pentland Firth regions in Scotland, where typical values range from approximately 1 m/s in general coastal regions to 3.5–4.5 m/s in high-current areas.

The natural frequency in air, obtained from decay tests, can serve as a basis to estimate the natural frequency in water [see Equation (1)],

$$f_{Nw} = f_{Na}[1 + (\pi C_a/4\mu)]^{-0.5} \quad (1)$$

where f_{Nw} is the natural frequency of the cable in water, where f_{Na} is the natural frequency of the cable in air, C_a is the added mass coefficient, and μ is the mass ratio (Vandiver, 1993). Then assuming an added mass coefficient C_a = 1, the natural frequency in water calculated using Eq. (1), resulted in approximately f_{Nw} = 0.41 Hz. Our free decay tests in water revealed substantial damping, primarily due to the low bending stiffness and mass ratio of the cable. Vandiver (1993) previously observed that the added mass fluctuates significantly with reduced velocity, ranging from negative to high positive values. Given this complexity, we therefore chose to use the natural frequency in air when determining the reduced velocity (*Ur*) as expressed in Equation (2),

$$U_r = U/(f_{Nw}D) \quad (2)$$

where *U* is the current speed and *D* is the diameter of the cable. Moreover, whereas the first mode of reduced velocity is commonly applied for rigid or straight members, this approach may be misleading for a flexible cable where higher modes could drive the response frequency. Mode decomposition becomes particularly challenging as the flexible cable moves in three dimensions, and so we believe that use of the natural frequency in air as a constant provides a more pragmatic approach. The free decay tests in water exhibited strong damping,

resulting in poor signal quality, which made it challenging to identify higher-order modes of the lazy wave configuration. When the cable was pulled and released, it was overdamped, further degrading the quality of the free decay signals. To complement this, we used OrcaFlex to estimate the modal frequencies of the lazy wave configuration to compare them with the response frequencies. Modal analysis of cable in Lazy wave configuration replicating experiment conditions, including buoyancy floats, was carried out using OrcaFlex to simulate the natural modes of the instrumented assembly. Table 3 presents the natural frequencies obtained from OrcaFlex, based on the bending stiffness determined from bend tests. The values indicate that the lazy wave configuration exhibits significantly lower modal frequencies and these can be used further to connect to the response frequencies. However, some data collected by the Qualisys system during free decay tests in still water yielded a natural frequency of 0.125 - 0.14 Hz, which matched the frequency f_2 obtained from the OrcaFlex simulations, as shown in Table 3.

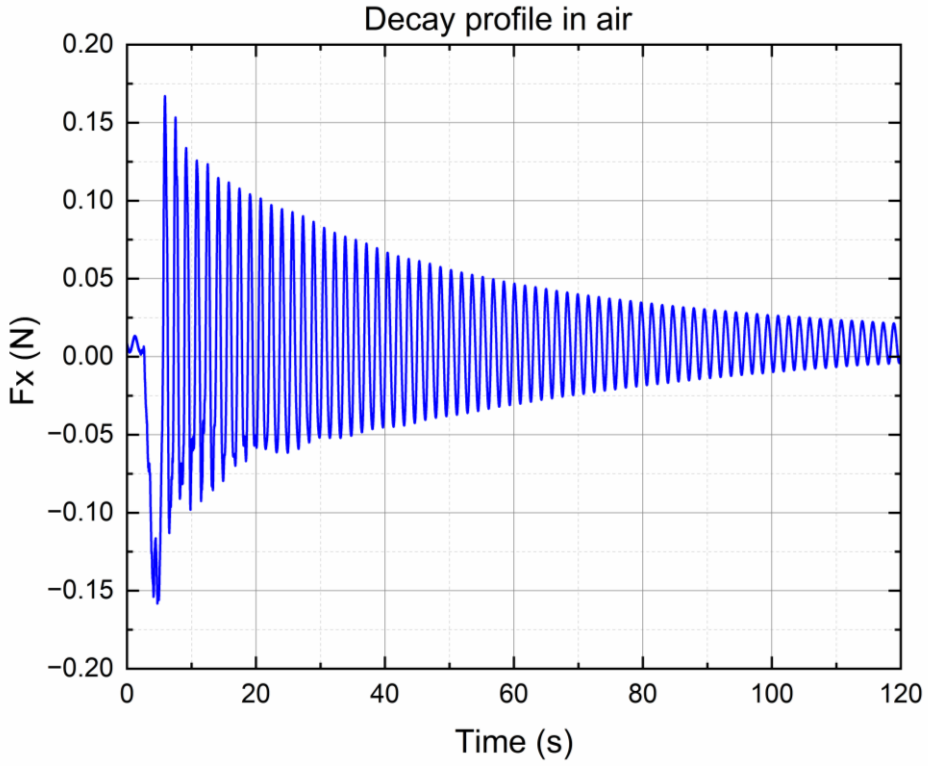

Figure 6: Force decay time history obtained from the load cell for the cable in air

Table 2: Cable properties

Bending stiffness, *EI*	0.217 Nm^2
Natural frequency in air, f_{Na}	0.61 Hz
Natural frequency in water, f_{Nw}	0.125-0.14 Hz

Table 3: Natural frequencies (f_{Nw}) predicted by modal analysis using OrcaFlex (all values in Hz).

f_1	f_2	f_3	f_4	f_5	f_6	f_7	f_8
0.0885	0.127	0.1857	0.2711	0.3034	0.4001	0.5174	0.6436
f_9	f_{10}	f_{11}	f_{12}	f_{13}	f_{14}	f_{15}	f_{16}
0.7256	0.911	0.9901	1.2248	1.2907	1.5763	1.6422	1.99

2.4 Cable in Lazy wave configuration

In still water, the cable adopted the lazy wave configuration (in the X-Z vertical plane) depicted in Figure 7(a) captured by the underwater camera. Note that in the vertical direction, Z = 0 and Z = 2 m respectively correspond to the tank floor and still water level. The cable profile, derived from Qualisys measurements, is plotted in Figure 7(b) and includes key features such as the top and bottom connections in the tank, the hang-off point, the sag bend, the buoyant section, the touchdown point, and the seven strain gauge locations (marked L1 to L7) along the cable. The markers M1 and M37 (Figure 7b) represent the top and bottom measurement points in the Qualisys system, which captures the cable profile. Before measuring the bending strain, the strain gauges were first calibrated in situ in still water.

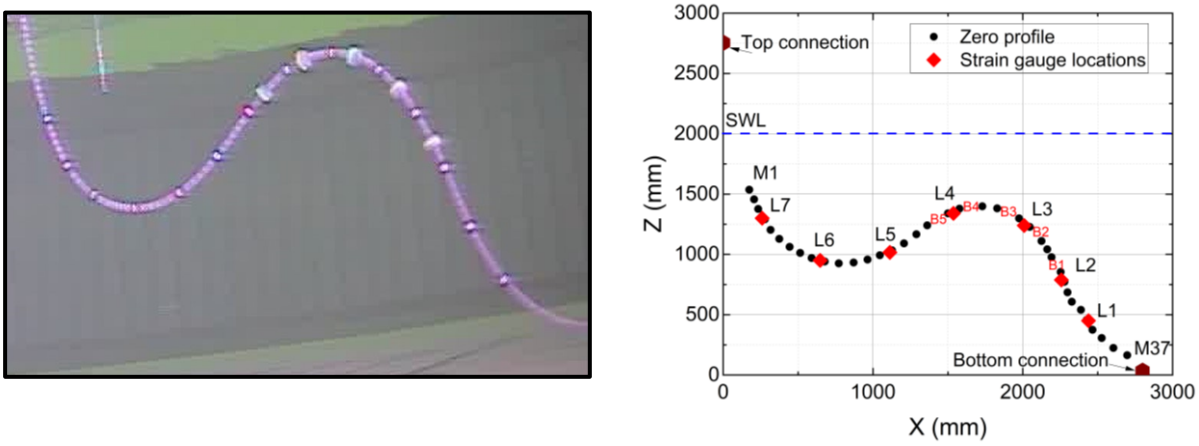

(a) (b)

Figure 7: Cable arrangement in FloWave: (a) photograph showing submerged cable in water; and (b) Cable position determined using Qualisys system showing strain gauge locations (L1 to L7) and the top and bottom connection points.

3. Results and Discussion

3.1 Test programme

Strain measurements were systematically acquired from each of the seven strain gauges along the length of the cable, for a current of speed ranging from 0.1 to 0.8 m/s. For each speed, the current propagation direction was altered from 0 to 180° in steps of 30°. Figure 8

depicts the current direction relative to the cable orientation in still water within the circular tank, in the global FloWave coordinate system. Table 4 summarizes the test conditions. Each set of measurements was collected for two minutes, after a 3-minute resting period between tests.

Table 4: Test Conditions listing current speeds, Reynolds number and reduced velocities

Tests	Current speed (m/s)	Reynolds number, Re	Reduced velocity, U_r
1	U1 = 0.1	3100	5.28
2	U2 = 0.2	6200	10.58
3	U3 = 0.3	9300	15.86
4	U4= 0.4	12400	21.15
5	U5 = 0.5	15500	26.44
6	U6 = 0.6	18600	31.72
7	U7 = 0.7	21700	37.02
8	U8 = 0.8	24800	42.30

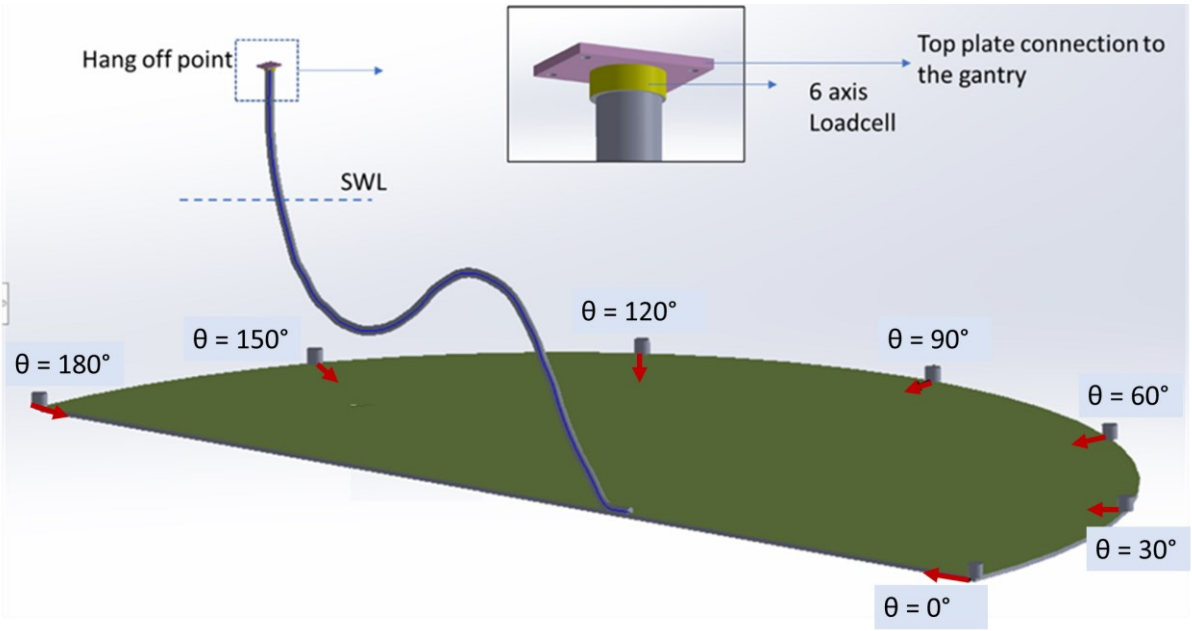

Figure 8: Schematic showing the cable alignment in the Edinburgh FloWave Facility and the direction of currents with respect to the cable.

3.2 Time-averaged deflections

Figure 9 presents profiles of the cable position in the XZ and XY planes as measured by Qualisys for increasing current speed and seven incident directions, θ = 0°, 30°, 60°, 90°, 120°, 150° and 180°, relative to the longitudinal axis of the cable. Figure 9 would help to visualise cable's deflection and thus expected to relate the displacements to measured strain. Measurements were recorded at multiple marker positions along the cable (from M1 at the top to M37 at the bottom), with the first marker, M1, initially positioned 1.5 m above the tank floor

(Z-axis) when the cable was placed in the tank in still water. Cable positions were measured relative to the initial position of zero profile without currents, enabling comparison of cable deflections at higher current speed. The profiles illustrate the movement of the cable relative to its initial zero-mean position in the (X-Z) plane, depicted by a solid black line, across different current directions and magnitudes. The cable is free to move in the current, except for its top end which is fixed to a load cell (see Figure 7(b) & 8), enabling the buoyancy region to shift forward and backward in response to current intensity. The fixed upper end of the cable at X = 0 caused a bend in the topmost portion of the cable ahead of the initial position of the first marker at top. Note that data points with unreliable Qualisys measurements have been removed from the plots. For θ = 0°, the cable adopts a lazy wave profile in the vertical plane close to the initial profile when U = 0.1 m/s. As the current speed increases, M1 is progressively pushed downward due to a combination of the topmost fixed-end condition and local bending by the cable to accommodate this in the XZ plane. The cable assumes an inclined profile from M1 to M37 near the touch-down point when U > 0.5 m/s. In the XY plane, the steady state profiles are slightly inclined, in keeping with the initial profile. For θ = 30° and 60°, the cable again alters its shape from a lazy wave profile to an almost straight configuration from M1 to M37 in the vertical XZ plane as the current speed is increased. Meanwhile, the upper portion of the cable undergoes increasing transverse displacement relative to the initial profile in the horizontal XY plane, appearing to bow increasingly outwards at higher current speeds. Although M37 remains almost fixed near the bed, M1 is displaced almost 1000 mm by the Y-component of the current. For θ = 90°, the cable again straightens from M1 to M37 in the XZ plane as the current speed increases and adopts the fundamental mode shape of a pinned structure. The cable undergoes maximum transverse displacement near its middle, reaching about 1600 mm when U = 0.8 m/s. For θ = 120° and 150°, as the current magnitude increases, the cable straightens from a higher point near the water surface. Marker M1 gets pulled downstream by the current. The touch-down end of the cable increasingly bows, and M37 is pulled away from M1 in the X-direction. In the horizontal plane, the upper portion of the cable is inclined whereas the lower portion bows outwards before inclining towards the bed. For θ = 180°, the current is directed along the cable longitudinal axis from the top to the bottom of the cable. As the current speed increases, the upper part of the cable straightens out becoming almost horizontal in the Y-Z plane. The lower portion of the cable increasingly bows out downstream. The near-bed vertical profile of the cable is concave for θ = 180° unlike θ = 0° where the near-bed vertical profile is convex. In the horizontal plane, the cable again adopts a slightly inclined profile like that of the initial profile, regardless of current speed. As would be expected, the Y-displacement of the cable is much smaller when the current is directed along the longitudinal axis of the cable (θ = 0° and 180°) than when the current is directed at an angle to the cable axis.

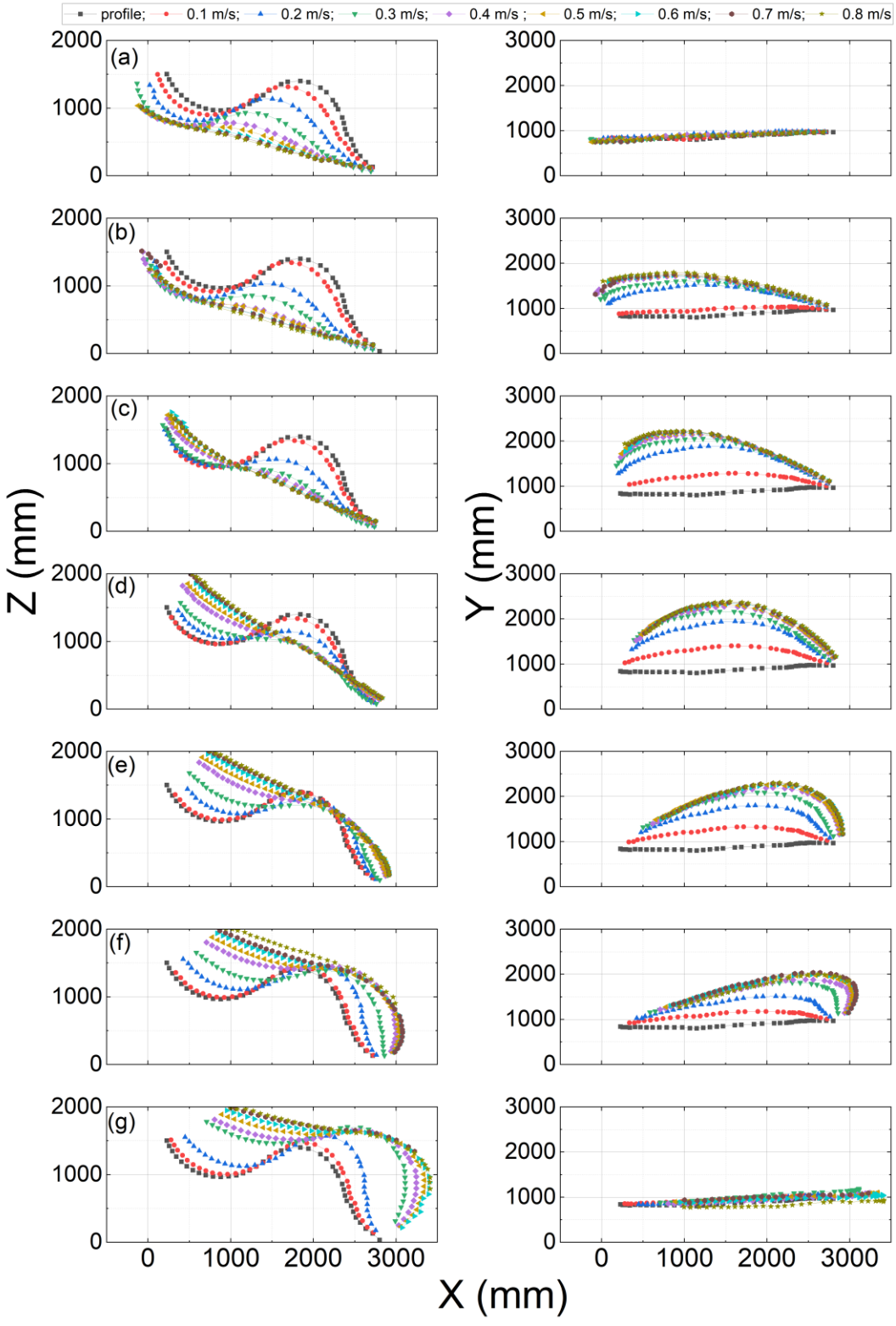

Figure 9: Lazy wave cable vertical XZ and horizontal XY profiles in a steady current of speed ranging from 0.1 to 0.8 m/s and direction: (a) θ = 0°; (b) θ = 30°; (c) θ = 60°; (d) θ = 90°; (e) θ = 120°; (f) θ = 150°; and (g) θ = 180°.

3.3 Cable curvature in steady current

As the measured strain is proportional to the curvature of the cable, we decided to present the results in terms of curvature. Appendix A describes our calculations of local curvature of different segments of the cable from the bending strain measurements using a full bridge Wheatstone connection. Recall that L1 is near the bottom end of the cable, L2 is adjacent to the first buoyancy module, L3 and L4 are positioned between the buoyancy modules, L5 and L6 are in the sagging bend region, and L7 is near the top of the cable. Figure 10 shows the curvature time histories obtained at all seven strain measurement locations for a current of speed U = 0.1, 0.3 and 0.5 m/s and direction θ = 0°. For the lowest current speed (Figure 10(a)), the cable curvature exhibits largest amplitude fluctuations at location L2 where bursting, highly cyclic behaviour is evident – symptomatic of localised vortex shedding. Hardly any curvature occurs at L3, L5, L6, and L7 due to flow shielding and the vortex suppression effect of the S-shape of the lazy cable. At L1 near the bed, significant low and higher frequency fluctuation is also evident, low frequency vibration perhaps related to the modal motion of the cable. For increased current speed of 0.3 m/s, the amplitude of curvature fluctuations increases everywhere along the cable (Figure 10 (b)). Although there is little further increase for a faster current speed of 0.5 m/s (Figure 10 (c)), the curvature time series contains more random fluctuations indicative of broader-band excitation. For all three current speeds considered, the increase in cable curvature at upper locations, L6 and L7, is lower than near the bed. Location L4 (near the top of the hump of the lazy cable between two buoyancy modules) undergoes larger amplitude, higher frequency vibrations compared to L3 and L5, highlighting the complicated local flow-structure interactions experienced by the cable as the current speed varies.

Figure 11 shows the local cable curvature time series obtained at Location L2 for three current speeds and seven directions. The responses for θ = 0° and 180° are significantly larger compared to other directions, indicating that the inline currents (θ = 0° and 180°) predominantly affect the curvature response of the lower part of the cable. Large temporal fluctuations in curvature are particularly evident for U = 0.5 m/s, especially for θ in the range from 90° to 180°.

For θ = 30° (see Figure 12), L4 shows greater variations in curvature compared to L2, as the inclined angle of the approaching current causes the upper portion of the cable to twist. The foregoing observations highlight the significant influence of current direction on the vibration response of a marine cable in an initially lazy wave configuration. The fluctuations in curvature are influenced by hydro-elastic behaviour of the cable which has an effective free length and shape that depends on the current direction relative to its longitudinal axis.

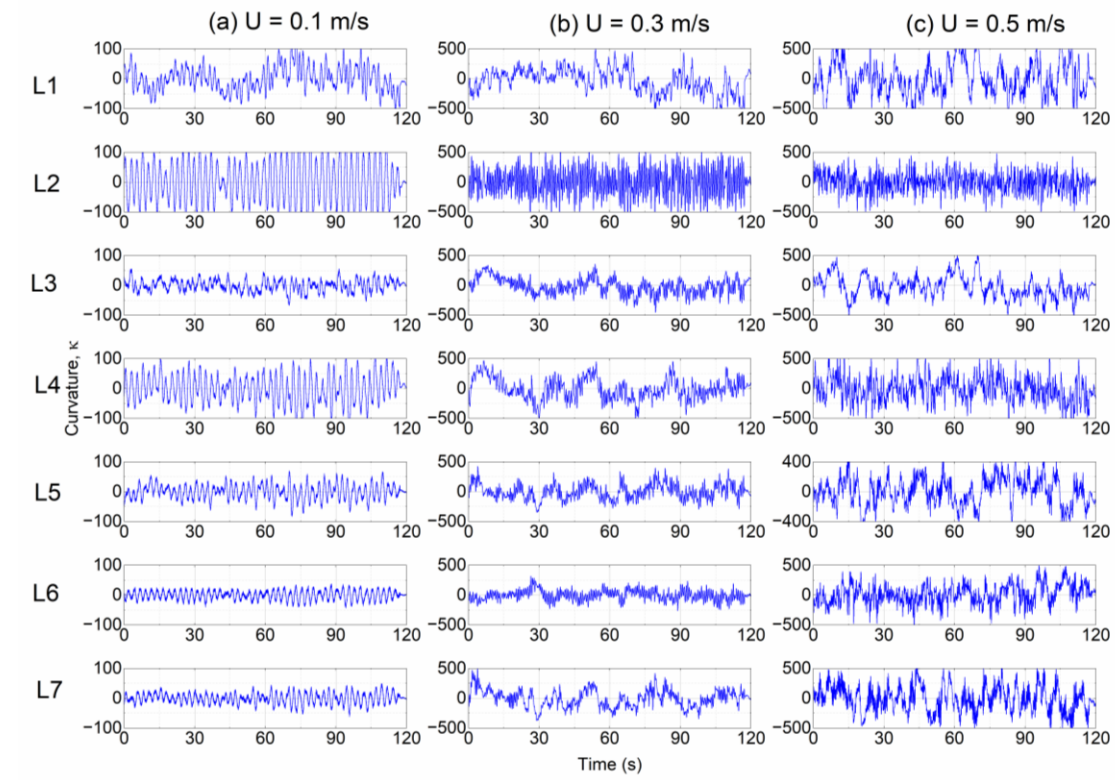

Figure 10: Cable curvature time history at Locations L1 to L7 for current of direction θ = 0° and speed: (a) U = 0.1 (b) U = 0.3 and U = 0.5 m/s.

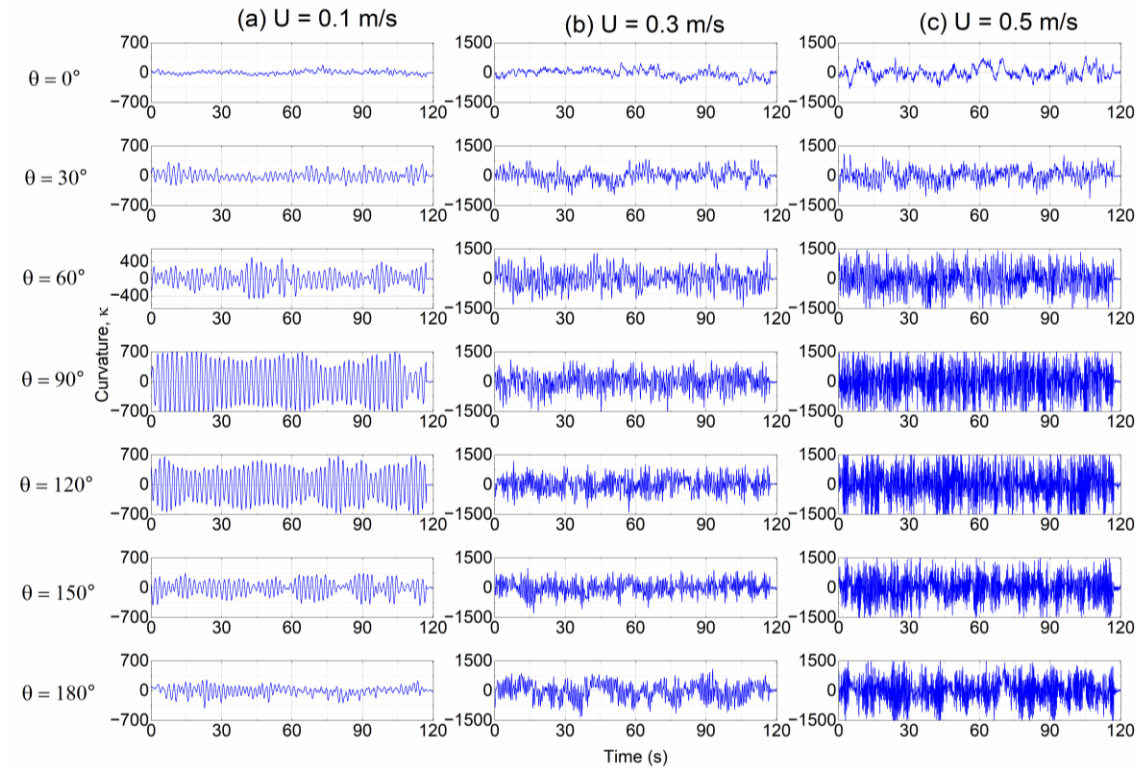

Figure 11: Cable curvature time history at Location L2 for a current of direction ranging from θ = 0° to 180° and speed: (a) U = 0.1 m/s, (b) U = 0.3 m/s, and U = 0.5 m/s.

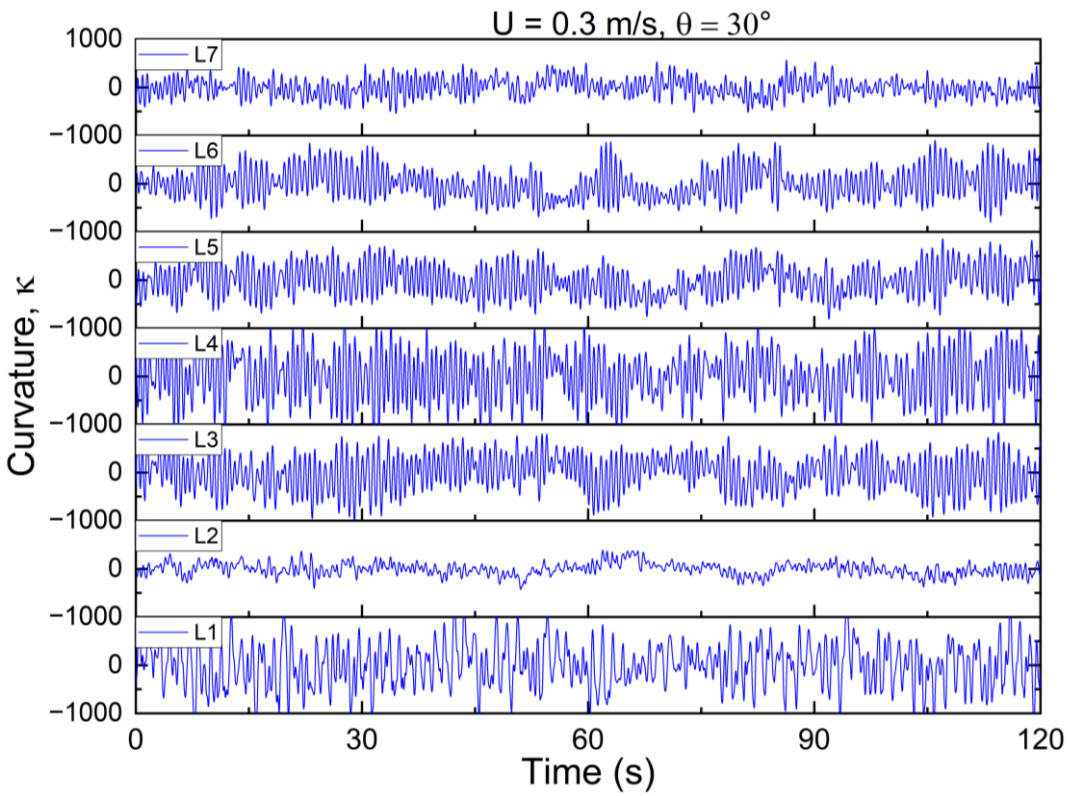

Figure 12: Cable curvature time history at locations L1 to L7 for a current of speed 0.3 m/s and direction, θ = 30°.

Figure 13 depicts the temporal standard deviation in curvature obtained at the seven strain-gauge locations for varying current speed and direction. The standard deviation in curvature is highly variable along the cable length, and largest at the near-bed location L1 for all current directions except θ = 0° and 30°. This elevated curvature at L1 is attributed to the strain experienced near the fixed support at the tank floor, especially when the current direction aligns with the initial longitudinal axis of the cable rather than opposing it. The highest variability in curvature occurs when the current acts almost perpendicular to the longitudinal axis of the cable. Low values of standard deviation occur near the top of the cable, indicating more stable curvature and potentially lower dynamic stresses. The relative difference in the values of κ_{std} appears to increase at most strain gauge locations along the cable as the current direction changes from θ = 0° to 90° (Figure 13 (a) to (d)), then progressively reduces from the upper part of the cable downwards until θ = 180° (Figure 13 (g)). In short, the variation in local bending strain is sensitive to the direction of current propagation.

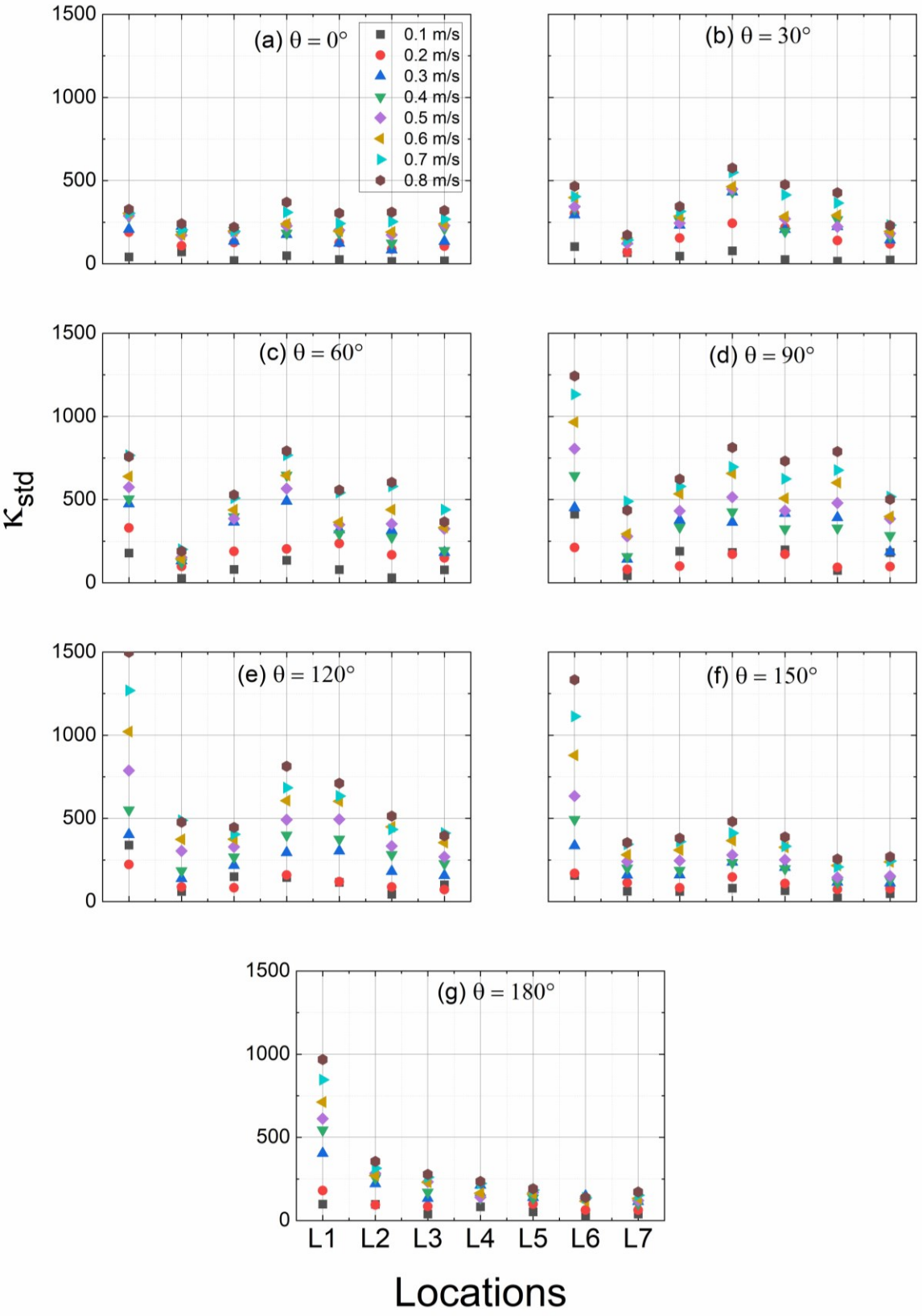

Figure 13: Cable profile with strain gauge locations showing the standard deviations of bending strain at increasing current velocities, U from 0.1 to 0.8 m/s for current directions (a) θ = 0°; (b) θ = 30°; (c) θ = 60°; (d) θ = 90°; (e) θ = 120°; (f) θ = 150°; and (g) θ = 180°.

3.4 VIV response frequencies

Spectral analysis of the curvature time series revealed the key vibration frequencies. Figure 14 shows the curvature spectra obtained at each strain gauge location when the cable was subjected to a current acting at θ = 180° and at speeds of 0.1, 0.3, 0.5 and 0.7 m/s. For the lowest current speed of 0.1 m/s, a spectral peak occurs at a single frequency f_{p} = 0.41 Hz at all locations (Figure 14 (a)). This peak corresponds to a Strouhal number of about 0.127 and is caused by vortex shedding from the cable. This peak is most pronounced at strain gauge L2. A second peak occurs at f_{p} = 0.56 Hz and is predominant at L1, L3, L4 and L5. This is due to complicated fluid-structure interactions near the bed and at the crest of the lazy cable, where the vortex shedding may perhaps be broader-band. When the current speed is increased to 0.3 m/s, the spectral peaks increase in amplitude by almost an order of magnitude (Figure 14 (b)). At all strain gauge locations except L5, there is a pronounced peak at f_{p1} ~ 1.4 Hz corresponding to the vortex shedding frequency at a Strouhal number of 0.145. At L5, the situation is more complicated with a relatively small primary peak at 1.75 Hz and several secondary peaks at about 1.1, 0.75, and 0.25 Hz, perhaps due to L5 lying in the wake of the upstream portion of the cable and the possible effect of travelling structural waves that propagate along the cable (with associated energy losses at the buoyancy modules and at bends in the lazy cable). L5 experiences the weakest response which is more broad-banded than elsewhere along the cable. When the current speed is increased further to 0.5 m/s, the curvature spectrum contains a distinct peak at about 2.3 Hz corresponding to a Strouhal number of about 0.14. This narrow-band vortex-shedding peak is dominant at L1, L2 and L6. The spectral energy is greatest at L1 in the lower part of the cable where vortex shedding is strongest. From L3 to L7 a second low-frequency peak can be seen at about 0.3 Hz at about twice the natural frequency of the cable in water. Between the two frequency peaks from L3 to L7 some small-amplitude broad-banded multi-peaked vibration is also evident (Figure 14 (c)). At a current speed of 0.7 m/s, most of the spectral response occurs at L1 and L2 due to pronounced vortex shedding at the lower region of the cable with a Strouhal number of about 0.14 (Figure 14 (d)). At all strain gauge locations, there is a small-amplitude peak at about 0.3 Hz and a further peak at about 1.8 Hz that reaches its maximum amplitude between L3 and L5. In general, the cable vibration seems dominated by vortex shedding at small values of current speed, but additional modes (possibly related to the fundamental natural frequency of the cable, Table 3) become activated at higher current speed. The dominant spectral peaks are usually larger at strain gauge locations near the bed than near the top of the cable.

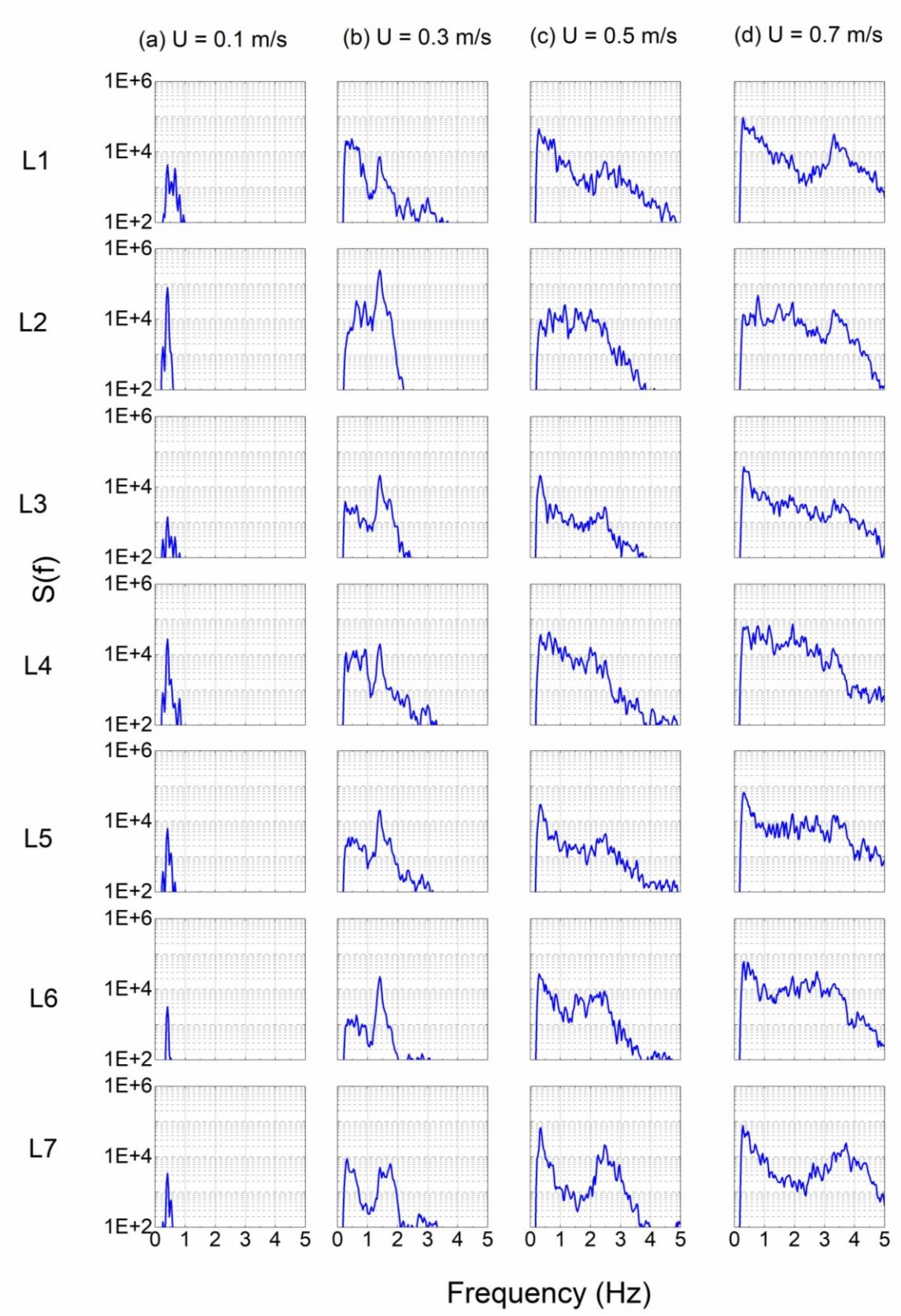

Figure 14: Spectral densities of curvature measured for a current direction of 180 degree and current velocities (a) U = 0.1 m/s (b) U = 0.3 m/s (c) U = 0.5 m/s and (d) U = 0.7 m/s at locations varying from L1 to L7 (Unit of S(f) = 1/Hz)

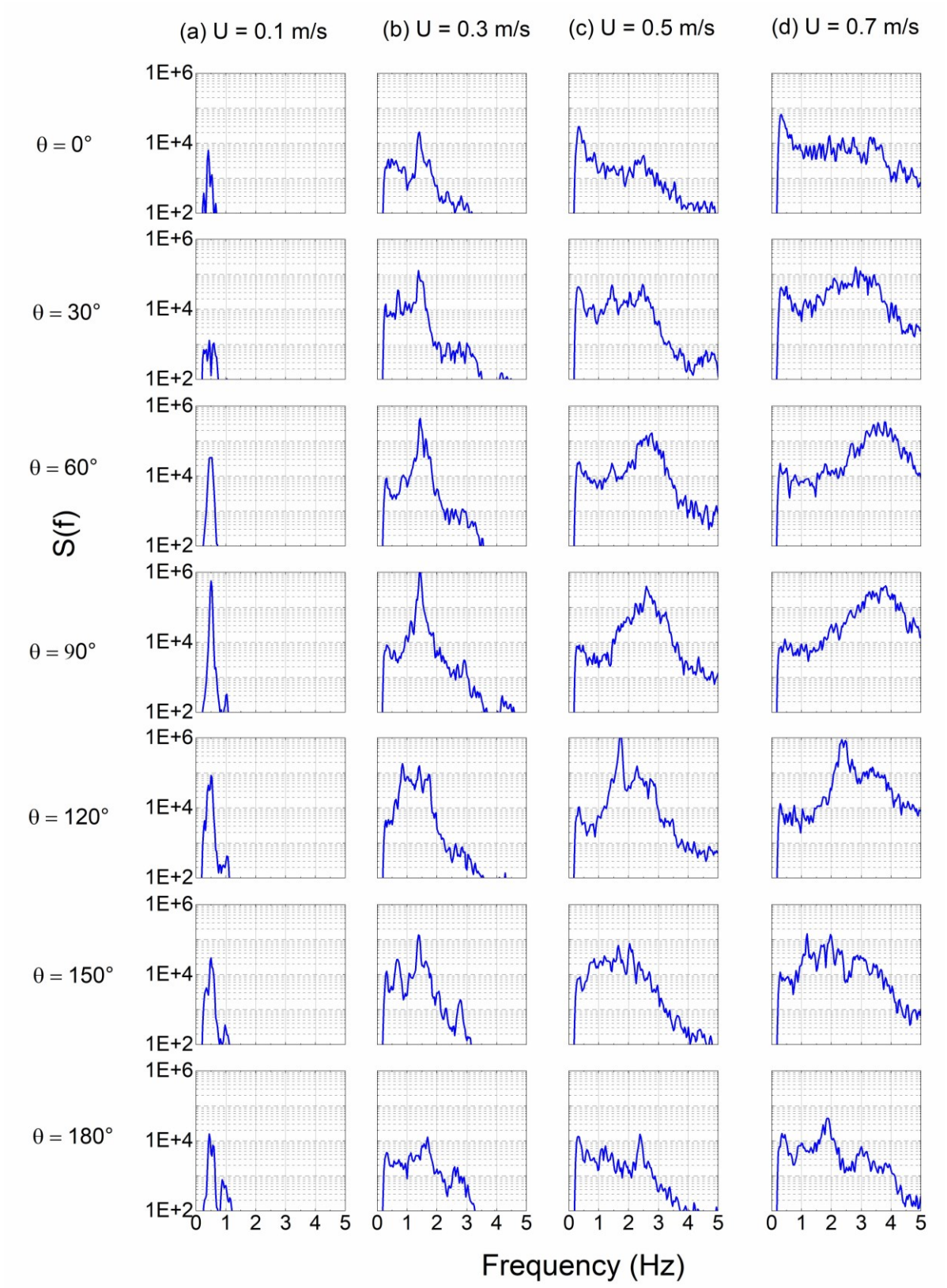

Figure 15: Spectral densities of curvature measured for current velocities (a) U = 0.1 m/s (b) U = 0.3 m/s (c) U = 0.5 m/s and (d) U = 0.7 m/s at location L5 for changing current directions from θ = 90° to 180° (unit of S(f) = 1/Hz)).

Figure 15 shows the curvature spectra at Location L5 at the sag bend of the cable when immersed in current of speed 0.1, 0.3, 0.5, and 0.7 m/s and direction θ = 0° to 180°. For the lowest current speed of 0.1 m/s, the spectral energy is invariably concentrated at the vortex shedding frequency at about 0.41 Hz, with largest response at θ = 90° when the current is incident perpendicular to the longitudinal axis of the lazy cable (Figure 15 (a)). However, as the current speed increases (Figures 15 (b) to (d)), notable changes take place to the spectral frequency content. The spectral peak consistently occurs at the Strouhal frequency when θ = 90° translating from 0.4 Hz for a flow speed of 0.1 m/s (Strouhal number of about 0.13) to about 3.8 m/s when the speed reaches 0.7 m/s (Strouhal number of about 0.14). Similar but broader-band behaviour can be seen for θ = 60° and 120°, but with lower, broader-band peak frequencies at θ = 60° and a lower narrower-band peak at a frequency of about 2.3 Hz for θ = 120° in a current of speed 0.7 m/s. For θ = 60° and 90°, the largest peak occurs as a single spike at the vortex shedding frequency when the current has a speed of 0.3 m/s. The highest peak for θ = 120° occurs when the current speed is 0.5 m/s. At higher flow speed, the spectral peak reduces in amplitude and becomes broader band. For θ = 180°, the spectrum contains low-amplitude components again related to vortex shedding and low-frequency modal behaviour. In short, when the current is normal to the cable axis, the dominant spectral curvature behaviour is narrow banded at the vortex shedding frequency. For all other current directions, the spectra are more complicated ranging from narrow-band single peaks at low current speed to broad-band multiple peaks at high current speed. This highlights the sensitivity of the lazy cable motions to the angle of approach of the current. For θ = 90°, the entire submerged length of the cable is exposed to the current acting normal to the longitudinal axis of the cable. For other current directions, the cable experiences inclined vortex shedding and shielding. As the current speed increases, the spectral energy tends to move to a higher frequency in accordance with a Strouhal number of about 0.13 - 0.145, except for θ = 0° where a single low frequency peak invariably occurs at about 0.25 Hz (about twice the first modal frequency of the cable, and about half its natural frequency in air).

Figure 16 provides a 3D representation of the spectral density variation as a function of frequency and reduced velocity for two values of current direction: θ = 0° (Figure 16 (a) & (b)), and θ = 90° (Figure 16 (c) & (d)). The visualization captures the distinct spectral behaviour between upper (L7) and lower (L1) locations along the cable. For θ = 0° at L7 (Figure 16 (a)) and L1 (Figure 16 (b)), the peak spectral energy remains concentrated at a frequency about twice the first modal frequency f_1 and grows in amplitude as the reduced velocity increases. A second smaller peak related to vortex shedding can also be discerned whose frequency increases as the reduced velocity increases. The most notable peak occurs at L1 for a reduced velocity of 10.57; there is no corresponding peak at L7. This is not the case for θ = 90°, where

both L1 (Figure 16 (c)) and L7 (Figure 16 (d)) experience their highest spectral peaks at a reduced velocity of 5.28 at a frequency of about 0.4 Hz. These maxima are due to flow-structure interaction when the vortex shedding frequency is about twice the natural frequency of the cable. At both L1 and L7, the spectral peak rapidly diminishes in amplitude as the reduced velocity increases to 10. With further increase in reduced velocity, the spectral peak associated with vortex shedding recovers and becomes larger-amplitude and broader-band. The spectral density is invariably much larger at L1 than L7, even though the key frequencies are similar. Noting the rapid change in spectral behaviour as the reduced velocity alters between 5.28 and 10.57, we recommend that further tests be conducted in future covering the reduced velocity range from 0 to 10.

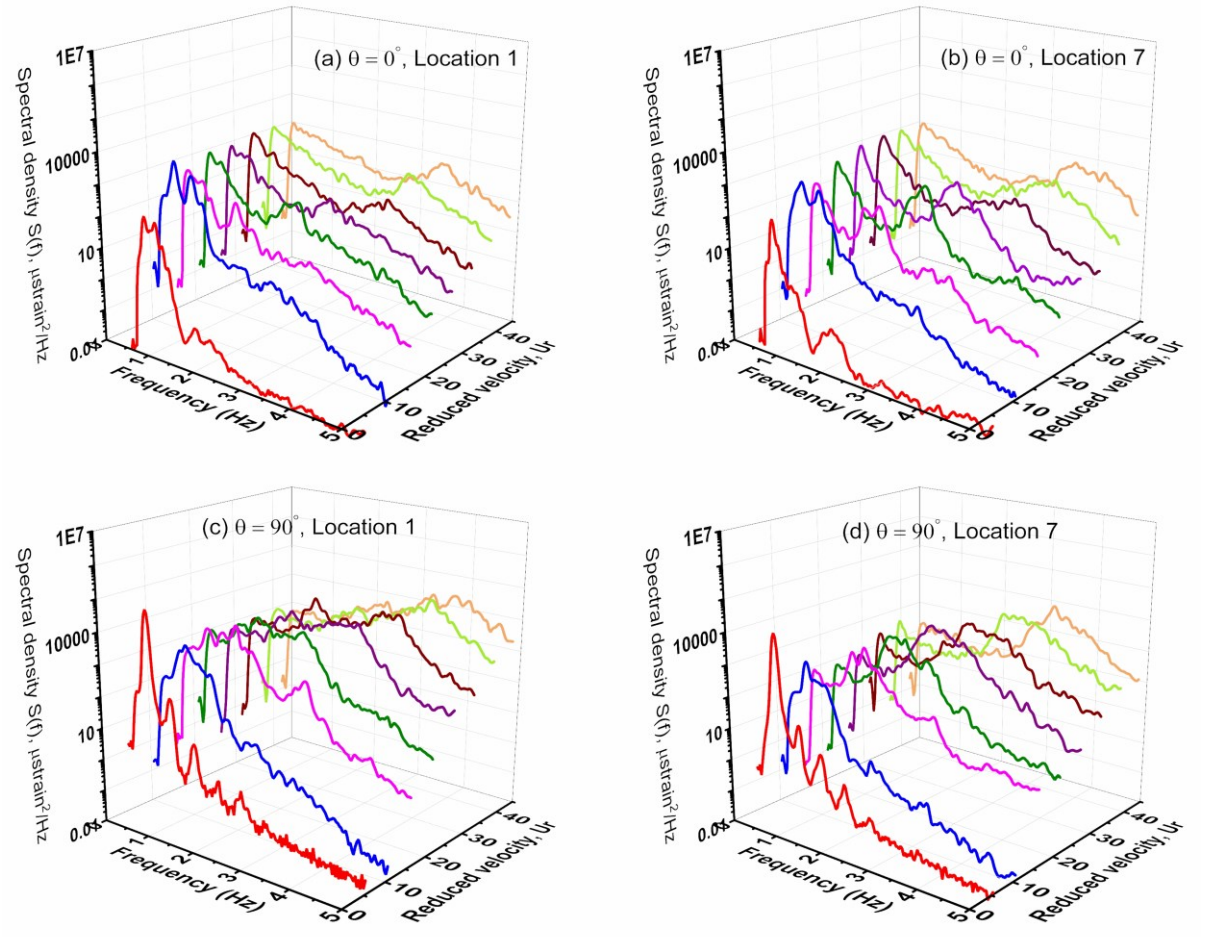

Figure 16: Spectral densities of curvature varying with reduced velocity for $\theta = 0°$ (a) Location 1 (b) Location 7 and for $\theta = 90°$ (c) Location 1 (d) Location 7.

3.5 Frequency analysis

Figure 17 plots the non-dimensional peak frequency $\hat{f}_p = f_{\mathrm{p}}D/U$ (in which f_{p} is the peak frequency) against the reduced velocity $U_r = U/f_{\mathrm{Na}}D$ where f_{Na} is the natural frequency of the cable in air. Here, we take the natural period of the cable in air to be f_{Na} = 0.61 Hz. The figure shows the results obtained at each strain gauge location for two current directions, with a line superimposed corresponding to a Strouhal number of 0.15. Although the Strouhal number ranges from 0.18 to 0.2 for vortex shedding from a rigid cylinder, its value has been found by Resvanis et al. (2012) to range from 0.13 to 0.14 for a long pipe in a uniform current within the critical flow regime (Re = 5000-220,000). Our experimental data reveal the Strouhal number for the lazy wave cable to lie between 0.127 and 0.145 for subcritical Reynolds numbers between 3,100 and 24,800. Figure 17 (a) shows $\hat{f}_p$ versus U_r for θ = 0°. In this case, $\hat{f}_p$ generally decreases as U_r increases. The non-dimensional peak frequency $\hat{f}_p$ approaches *St* = 0.14 at L4 and L5 when U_r is 10.57, at L2, L3, L4, L5, and L6 when U_r is 15.86, and at L2 when U_r is 21.15. For θ = 90° (Figure 17 (b)), $\hat{f}_p$ invariably lies between 0.1 and 0.18, indicating that vortex-shedding is taking place. The non-dimensional peak frequency varies along the cable being affected by the complicated (and perhaps loosely correlated) vortex shedding behaviour along the cable.

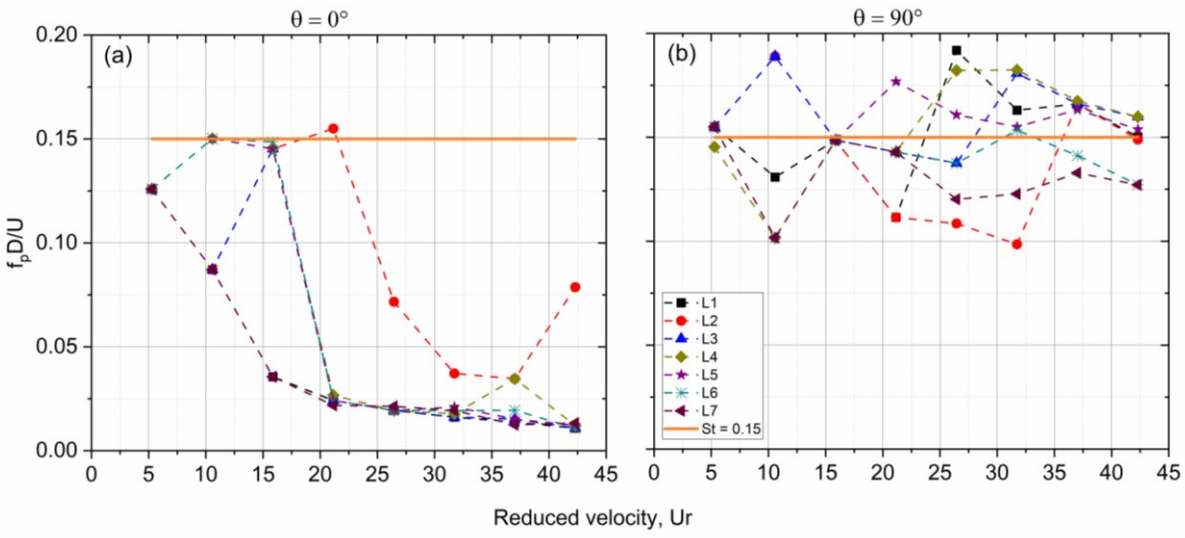

Figure 17: Variation in non-dimensional peak frequency $\hat{f}_p = f_{\mathrm{p}}D/U$ with reduced velocity $U_r = U/f_{\mathrm{Nw}}D$ at all strain gauge locations for current direction: (a) θ = 0°; and (b) θ = 90°.

Figure 18 shows the dependence of the peak frequency ratio $f_{\mathrm{p}}/f_{\mathrm{Na}}$ at each strain gauge location on reduced velocity $U_r = U/f_{\mathrm{Na}}D$ for the different current directions. For θ = 0°, at the lowest U_r = 5, the peak frequency ratio of almost unity accords with a Strouhal number of 0.15 (the amber line in Figure 18). As increases, the peak frequency ratio falls to about half

indicating that the response is essentially a structural mode at about half the natural frequency in air (Modal frequency f_5, Table 3). For θ = 0°, 30° and 60°, f_p/f_{Na} at L1 gradually increases until it exceeds 2 (Figure 18 (a)) and follows the Strouhal line for all other current directions as U_r increases. At Location L2 (Figure 18 (b)), the frequency ratio behaviour is roughly similar to that at L1, with f_p/f_{Na} following the Strouhal line until U_r reaches ~ 21. At higher U_r, the frequency ratio is direction-dependent and seems to have an upper bound at the Strouhal line. This is also the case for Locations L3 to L7 (Figure 18 (c) to (g)). At most locations the results for θ = 180° are quite different to those for θ = 0° with the former following the Strouhal line and the latter corresponding to half the natural frequency in water. This behaviour has also been observed in other laboratory tests undertaken by Assi et al. (2014) and Chaplin & King (2018) whereby the cable adopts a concave profile when θ = 180° and exhibits higher vibration amplitude at the cable bottom, unlike its convex counterpart when θ = 0°. Moreover, Jain & Modarres-Sadeghi (2013) have reported that the peak frequency reduces when the cylinder is oriented at a large angle of inclination to the tank floor, a phenomenon also observed herein when θ = 0°. For this current direction, the cable progressively inclines towards the tank floor as U_r is increased, simultaneously aligning the top portion of the cable vertically to the flow. This explains the reduction in peak frequency observed for θ = 0° and when the cable has a large angle of inclination to the bed. By contrast, for θ = 180°, the upper portion of the cable stretches out to form a nearly horizontal profile, while the lower part of the cable aligns itself almost perpendicular to the tank bottom. At Location L7, the peak frequency ratio reduces in both the θ = 0° and 180° directions where the current is aligned with the longitudinal axis of the cable. As U_r increases, the peak frequency ratio further diminishes for θ = 30°, 150° and θ = 180°. At normal incidence when θ = 90°, the cable responds strongly at the vortex shedding frequency. Previous literature (Assi et al., 2006; Morooka & Tsukada, 2013; Vandiver et al., 2009) has reported lock-in and resonance behaviour primarily within the reduced velocity range of 4 to 8. However, as U_r increases, the peak frequency ratio exhibits complicated behaviour influenced by both the current magnitude and its direction. In a previous study, Chaplin et al. (2005) found that there was a decrease in response at higher U_r due to the establishment of different combinations of modes. In the present study, a similar modal effect was observed at higher reduced velocities (U_r). The variation in vibration response is attributed to the changing orientation and inclination of the cable due to current-induced forces, which alter the local flow conditions along its length (current not normal to the cable at all times). At certain locations, the dominant frequencies align with the Strouhal frequency, indicating the presence of vortex-induced vibrations (VIV). However, as the reduced velocity increases, the vibration response shifts, and the dominant frequencies begin to follow the system's natural modal frequencies. Specifically, at elevated U_r, the lower observed frequency

ratio (f/f_{Na} = 0.511) corresponds to the fifth modal frequency (f_5 = 0.3034 Hz) as presented in Table 3. This highlights the coexistence of VIV and structural modal responses, influenced by the complex interaction between hydrodynamic loading and the flexible lazy wave configuration.

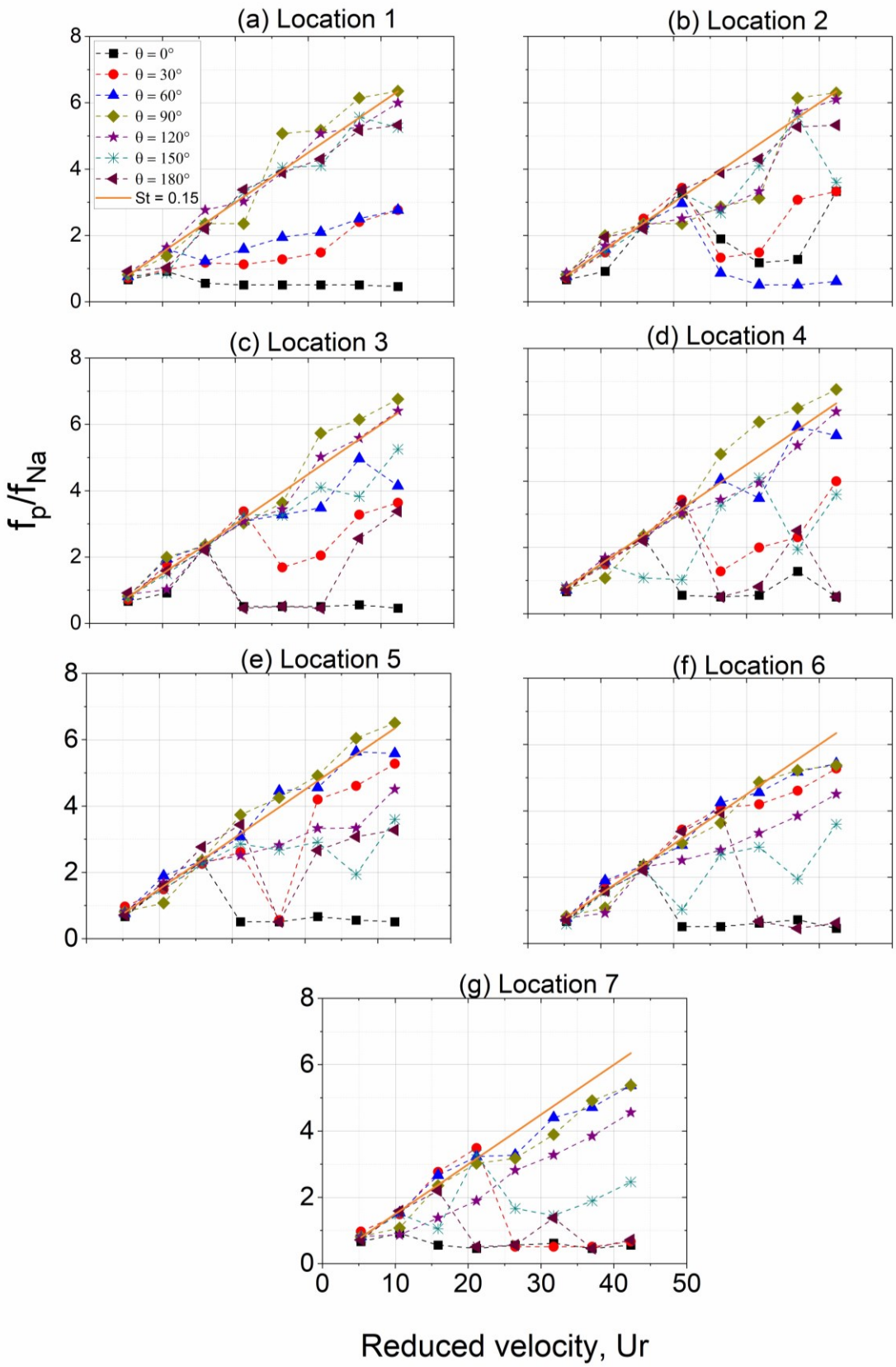

Figure 18: Variation in frequency ratio $f_{\mathrm{p}}/f_{\mathrm{Nw}}$ with reduced velocity $U_r = U/f_{\mathrm{Nw}}D$ and different current directions at strain gauge locations: (a) L1; (b) L2; (c) L3; (d) L4; (e) L5; (f) L6; and (g) L7.

3.6 Time-frequency analysis

Continuous wavelet transforms (CWT) time-frequency analysis of the curvature signals for increasing current velocities at varying locations along the depth was carried out to analyse the frequency sharing and mode transitions. Figure 19 presents the resulting CWT strain scalograms at Location L4 of the lazy cable in a steady current of direction θ = 0° and speed ranging from 0.1 to 0.8 m/s. At the lowest current speed of 0.1 m/s (U_r = 5.27), the local response is concentrated at a single frequency corresponding to f/f_{Na} = 1 and persists at all times (Figure 19 (a)). Increasing the current speed to 0.2 m/s, the response occurs at two frequencies corresponding to f/f_{Na} = 1 and 2 (Figure 19 (b)); the first frequency component is intermittent whereas the second is almost continuous. As the current speed increases to 0.6 m/s and more (Figures 19 (d), (e) & (f)), multiple frequency components occur at integer multiples of f/f_{Na} from 1 to 4 in the wavelet plots. The intensity and multiplicity of the peaks increases with current speed as is evident in Figures 19 (g) & (h). The lowest frequency peak of f/f_{Na} = 1 weakens considerably with current speed and eventually almost disappears by *U* = 0.7 m/s. The next-lowest frequency peak of f/f_{Na} = 2 has almost vanished by U = 0.9 m/s. The CWT strain scalograms indicate that the response becomes stronger but more intermittent and the dominant frequency shifts to higher integer-multiple values of the natural frequency in air as the current speed increases for θ = 0°.

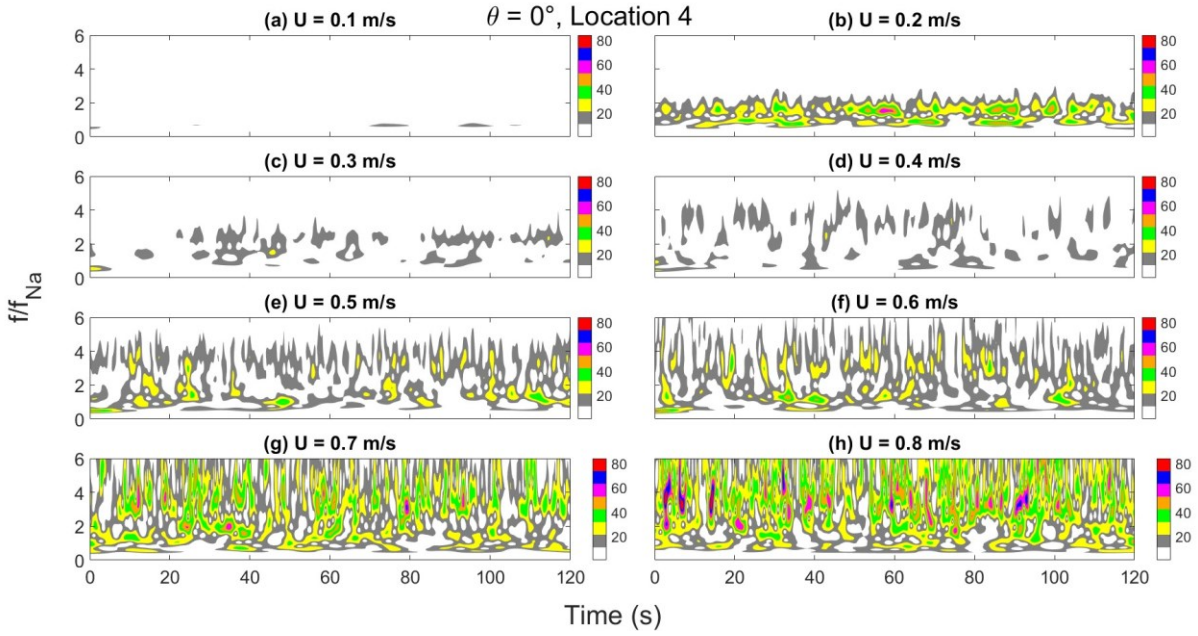

Figure 19: Wavelet plot showing contours of spectral density as a function of frequency ratio and time at Location L4 in current of direction θ = 0° and speed: (a) 0.1 m/s; (b) 0.2 m/s; (c) 0.3 m/s; (d) 0.4 m/s; (e) 0.5 m/s; (f) 0.6 m/s; (g) 0.7 m/s; (h) 0.8 m/s.

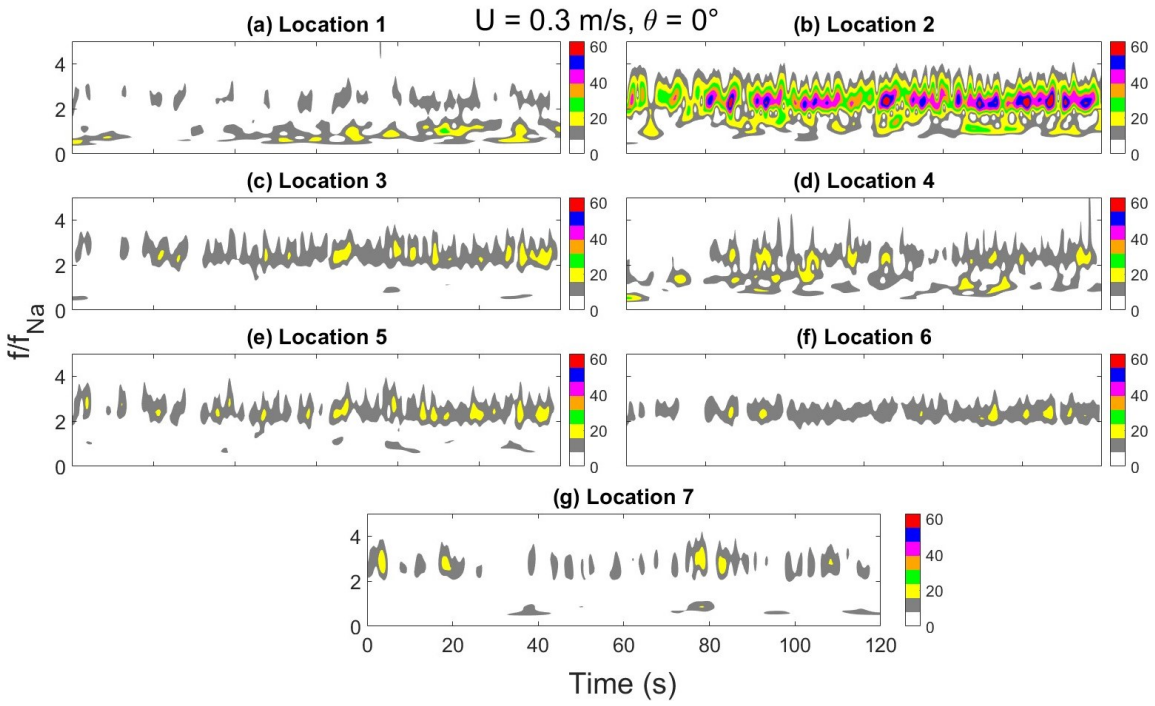

Figure 20: Wavelet plot showing contours of spectral density as a function of frequency ratio and time in current of direction θ = 0° and speed 0.3 m/s at locations: (a) L1; (b) L2; (c) L3; (d) L4; (e) L5; (f) L6; and (g) L7.

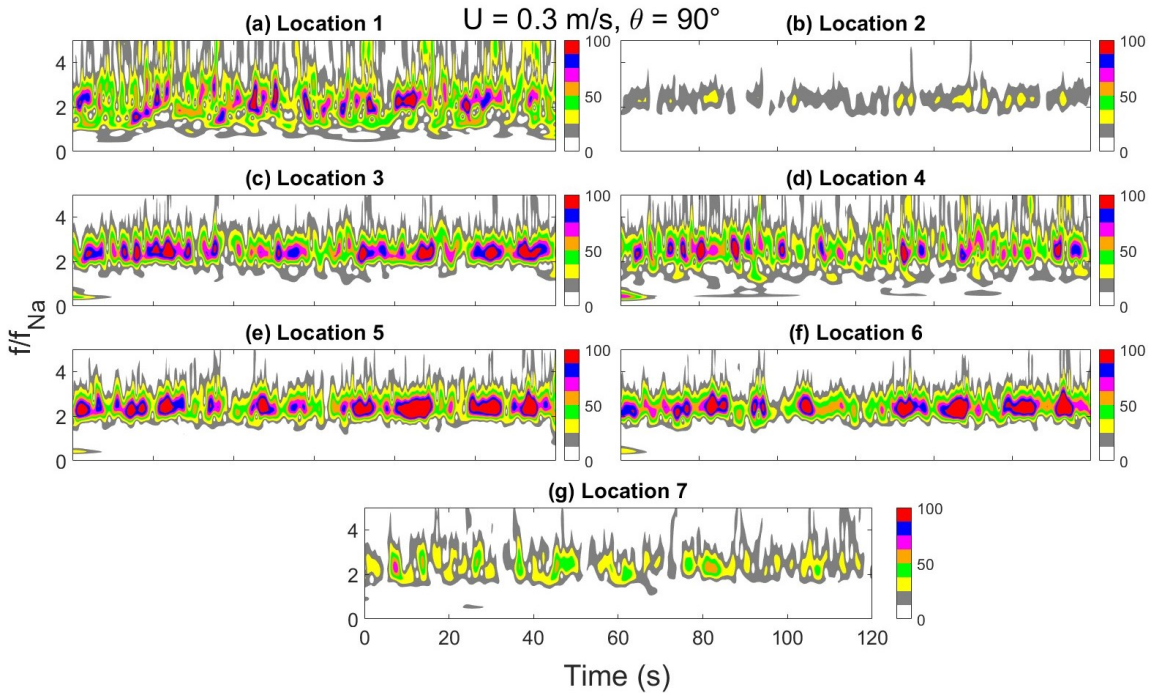

Figure 21: Wavelet plot showing contours of spectral density as a function of frequency ratio and time in current of direction θ = 90° and speed 0.3 m/s at locations: (a) L1; (b) L2; (c) L3; (d) L4; (e) L5; (f) L6; and (g) L7.

Figure 20 presents the CWT strain scalograms at locations L1 to L7 along the cable when subject to a current of speed 0.3 m/s acting at θ = 0°. At L1 (Figure 20 (a)), energy is intermittently concentrated at f/f_{Na} = 0.4 and 1, indicating some excitation by vortex shedding and structural vibration at a fundamental mode. At L2 (Figure 20(b)), the spectral density distribution has altered so that it contains a more pronounced peak at $f/f_{\mathrm{Na}} \approx 2$ and an increase in magnitude, associated with VIV. At L3 (Figure 20 (c)), the frequency response is similar to but much smaller than to L2. At L4 (Figure 20 (d)), located at the crest of the initial lazy cable, the strain spectral density distribution broadens with significant frequency components at f/f_{Na} = 0.4, 1, and 2 (see also the spectrum in Figure 14). By contrast, the strain spectral density at locations L5 and L6 (Figures 20 (e) and 20 (f)) near the top of the buoyancy section of the cable is greatly reduced and mainly at a frequency f/f_{Na} = 2. At L7 near the top of the cable (Figure 20 (g)), the strain spectral density is further reduced and intermittent, acting mainly at f/f_{Na} = 3, and partly at f/f_{Na} = 0.4. In general, the spectral strain density is weaker near the top and bottom of the cable, but much more pronounced at the bends and buoyancy modules of the lazy cable, perhaps indicating the presence of modal vibrations that travel along this region of the cable.

Figure 21 presents the CWT strain scalograms at locations L1 to L7 along the cable when subject to a current of speed of 0.3 m/s directed at θ = 90°. Unlike when the current is aligned with the longitudinal axis of cable (θ = 0°), the perpendicular current greatly increases the magnitude of the strain spectral density distribution along the whole length of the immersed cable. At all locations along the cable, except L2 and L7, the spectral density retains a strong, nearly continuous peak at about f/f_{Na}= 2 throughout the time interval considered, associated with persistent, strong vortex shedding.

In all cases, the variation in frequency over time is evident, with multiple frequencies gaining strength at higher reduced velocities. This indicates a chaotic, non-stationary VIV response, where no clear lock-in phenomenon is observed in the flexible cable. Further analysis of displacements in the inline and cross-flow direction will provide deeper insights into vibration frequencies, as well as trajectory patterns. This may help identify potential lock-in scenarios that could develop under specific conditions

4. Conclusions

Comprehensive measurements have been made of the time-dependent local bending strain on a laboratory scale model of a slender hydro-elastic marine power cable in a lazy wave configuration. The cable had a small diameter of 31 mm, low bending stiffness, and mass ratio of 1.22. Bending strains at seven locations along the cable were interpreted in terms of flow-induced vibrations and natural modal behaviour of the cable when immersed in a steady

current. A parameter study was undertaken in which the speed of the current was varied from 0.1 to 0.8 m/s and its direction varied from 0 to 180 degrees with respect to the initial longitudinal axis of the cable. The Reynolds number range spanned from 3,100 to 24,800 and the reduced velocity based on natural frequency in air was varied from 5.28 to 42.30. The results shed new light on the complicated strain behaviour of a lazy wave power cable in a steady current. The main findings are as follows:

- In all cases, the bending curvature exhibits larger temporal fluctuations near the touch down point of the lazy cable than at the top. For a current direction that is neither exactly along nor normal to the longitudinal axis of the cable, other locations along the cable, such as the sag and hogging points, also experience significant variations in curvature.
- The magnitude of cable curvature increases sharply as the reduced velocity increases from 5.28 to 15.86. At higher current speeds, although the variation in curvature persists, it starts to fluctuate randomly and is less correlated with increasing current speed.
- Bending strain spectra reveal localized dynamic changes in peak frequency content as the current speed increases. Peak curvature magnitude and frequencies are consistently higher at cable locations near the bed and progressively decrease toward the top of the cable as the current speed increases. At higher reduced velocity (U_r > 15.86), the spectral strain density becomes broader band with additional secondary peaks developing in the spectrum in the upper portion of the cable. These may be associated with complicated modal behaviour due to the cable configuration and viscous losses caused by the bluff-body buoyancy modules.
- The bending strain spectra are very sensitive to the oncoming current direction. For a current normal to the longitudinal axis of the cable, vibrations occur at higher frequencies regardless of current magnitude. In this case, the entire length of the cable is exposed to the flow, and there is no shielding or blockage effect. Conversely, when the longitudinal axis of the cable is aligned with the current direction, minimal frequency shifts occur with changing current speed.
- In general, the cable vibrations correspond to peak frequencies normalized by cable diameter and current speed that fall within a range of 0.127 to 0.145 in accordance with the Strouhal number. Along the cable, certain locations exhibit strain frequencies that observe a linear trend corresponding to the Strouhal number, whereas other locations experience very low peak frequencies related to the modal behaviour of the cable. The frequency ratio f_p/f_{Na} increases with reduced velocity based on the natural frequency in air when the current direction is normal to the longitudinal axis of the cable; otherwise f_p/f_{Na} <1 for other current directions depending on the measurement location. For the cases considered herein, lock-in behaviour is not evident.

- Time-frequency analysis reveals that the strain response alters from a single frequency to multiple frequencies as the reduced velocity increases. A high-magnitude low-frequency peak is evident, though it does not persist over time. Frequency sharing is observed at higher current speeds. As the reduced velocity increases, the curvature is affected by the superposition of low frequency modes. Multiple frequencies occur, especially when the current is neither exactly normal or parallel to the longitudinal axis of the cable.

This study has demonstrated the importance of considering current directionality and cable location when assessing the bending strain on a lazy wave marine cable. Critical areas prone to damage include locations near the touchdown zone and the sag bend. In our tests, a current direction between 30 and 120 degrees appears important in promoting fatigue damage. In the future, we intend to undertake a more holistic analysis of the forces, strains, and displacements measured in our physical model tests to gain further insight into the flow-induced vibration of a marine power cable. We believe that the findings presented herein should be of considerable use to modellers and designers of marine power cables.

ACKNOWLEDGEMENTS

The authors are grateful for financial support from the UK Engineering and Physical Sciences Research Council through CableDyn: Subsea Power Cable Dynamics Under Complex Ocean Environment (EP/W015102/1). Special thanks are extended to Narakorn Srinil and Rameez Badhurshah (Newcastle University), Philipp Thies and Faryal Khalid (University of Exeter), for their valuable discussions and active participation in the experimental investigations conducted at FloWave

References

Assi, G. R. S., Srinil, N., Freire, C. M., & Korkischko, I. (2014). Experimental investigation of the flow-induced vibration of a curved cylinder in convex and concave configurations. *Journal of Fluids and Structures*, *44*, 52–66. https://doi.org/10.1016/j.jfluidstructs.2013.10.011

Chaplin, J. R., Bearman, P. W., Huera Huarte, F. J., & Pattenden, R. J. (2005). Laboratory measurements of vortex-induced vibrations of a vertical tension riser in a stepped current. *Journal of Fluids and Structures*, *21*(1 SPEC. ISS.), 3–24. https://doi.org/10.1016/j.jfluidstructs.2005.04.010

Chaplin, J. R., & King, R. (2018). Laboratory measurements of the vortex-induced vibrations of an untensioned catenary riser with high curvature. *Journal of Fluids and Structures*, *79*, 26–38. https://doi.org/10.1016/j.jfluidstructs.2018.01.008

Fan, Y. ting, Mao, H. ying, Guo, H. yan, Liu, Q. hai, & Li, X. min. (2015). Experimental investigation on vortex-induced vibration of steel catenary riser. *China Ocean Engineering*, *29*(5), 691–704. https://doi.org/10.1007/s13344-015-0049-4

Franzini, G. R., Pesce, C. P., Gonçalves, R. T., Fujarra, A. L. C., & Mendes, P. (2016). Experimental Investigations on Vortex-Induced Vibrations with a Long Flexible Cylinder. Part I: Modal-Amplitude Analysis with A Vertical Configuration. *11th International Conference on Flow-Induced Vibration, Hagues*.

Govardhan, R. N., & Williamson, C. H. K. (2006). Defining the “modified Griffin plot” in vortex-induced vibration: Revealing the effect of Reynolds number using controlled damping. *Journal of Fluid Mechanics*, *561*, 147–180. https://doi.org/10.1017/S0022112006000310

Greenwood, C., Vogler, A., & Venugopal, V. (2019). On the variation of turbulence in a high-velocity tidal channel. *Energies*, *12*(4). https://doi.org/10.3390/en12040672

Huera-Huarte, F. J., & Bearman, P. W. (2009). Wake structures and vortex-induced vibrations of a long flexible cylinder-Part 1: Dynamic response. *Journal of Fluids and Structures*, *25*(6), 969–990. https://doi.org/10.1016/j.jfluidstructs.2009.03.007

Jain, A., & Modarres-Sadeghi, Y. (2013). Vortex-induced vibrations of a flexibly-mounted inclined cylinder. *Journal of Fluids and Structures*, *43*, 28–40. https://doi.org/10.1016/j.jfluidstructs.2013.08.005

Lie, H., & Kaasen, K. E. (2006). Modal analysis of measurements from a large-scale VIV model test of a riser in linearly sheared flow. *Journal of Fluids and Structures*, *22*(4), 557–575. https://doi.org/10.1016/j.jfluidstructs.2006.01.002

Martinelli, L., Lamberti, A., Ruol, P., Ricci, P., Kirrane, P., Fenton, C., & Johanning, L. (2010). Power Umbilical for Ocean Renewable Energy Systems-Feasibility and Dynamic Response Analysis. *3rd International Conference on Ocean Energy, 6th October, Bilbao*. https://www.researchgate.net/publication/228814942

Moideen, R., Venugopal, V., & Chaplin, J. (2024). Vortex Induced Vibrations of a Lazy Wave Dynamic Power Cable Under Various Currents and Propagation Directions: Analysis Of Strain. http://asmedigitalcollection.asme.org/OMAE/proceedings-pdf/OMAE2024/87851/V007T09A037/7361615/v007t09a037-omae2024-126678.pdf

Morooka, C. K., & Tsukada, R. I. (2013). Experiments with a steel catenary riser model in a towing tank. *Applied Ocean Research*, *43*, 244–255. https://doi.org/10.1016/j.apor.2013.10.010

Pereira, F. R., Gonçalves, R. T., Pesce, C. P., Fujarra, A. L. C., Franzini, G. R., & Mendes, P. (2013). A Model Scale Experimental Investigation on Vortex-Self Induced Vibrations (VSIV) Of Catenary Risers. http://asmedigitalcollection.asme.org/OMAE/proceedings-pdf/OMAE2013/55416/V007T08A029/4431779/v007t08a029-omae2013-10447.pdf

Pesce, C. P., Franzini, G. R., C Fujarra, A. L., Gonçalves, R. T., Salles, R., Mendes Riser, P., & Engineering, F. (2017). Further Experimental Investigations on Vortex Self-Induced Vibrations (VSIV) with A Small-Scale Catenary Riser Model. http://journals.asmedigitalcollection.asme.org/OMAE/proceedings-pdf/OMAE2017/57649/V002T08A016/2532750/v002t08a016-omae2017-62100.pdf

Raghavan, K., & Bernitsas, M. M. (2011). Experimental investigation of Reynolds number effect on vortex induced vibration of rigid circular cylinder on elastic supports. *Ocean Engineering*, *38*(5–6), 719–731. https://doi.org/10.1016/j.oceaneng.2010.09.003

Rentschler, M. U. T., Adam, F., & Chainho, P. (2019). Design optimization of dynamic inter-array cable systems for floating offshore wind turbines. *Renewable and Sustainable Energy Reviews*, *111*, 622–635. https://doi.org/10.1016/j.rser.2019.05.024

Rentschler, M. U. T., Adam, F., Chainho, P., Krügel, K., & Vicente, P. C. (2020). Parametric study of dynamic inter-array cable systems for floating offshore wind turbines. *Marine Systems and Ocean Technology*, *15*(1), 16–25. https://doi.org/10.1007/s40868-020-00071-7

Resvanis, T. L., Jhingran, V., Vandiver, J. K., & Liapis, S. (2012). Reynolds Number Effects on the Vortex-Induced Vibration of Flexible Marine Risers. *Proceedings of the ASME 2012 31st International Conference on Ocean, Offshore and Arctic Engineering OMAE2012 July 1-6, 2012, Rio de Janeiro, Brazil*.

Sarpkaya, T. (2004). A critical review of the intrinsic nature of vortex-induced vibrations. *Journal of Fluids and Structures*, *19*(4), 389–447. https://doi.org/10.1016/j.jfluidstructs.2004.02.005

Sutherland, D. R. J., Noble, D. R., Steynor, J., Davey, T., & Bruce, T. (2017). Characterisation of current and turbulence in the FloWave Ocean Energy Research Facility. *Ocean Engineering*, *139*, 103–115. https://doi.org/10.1016/j.oceaneng.2017.02.028

Thies, P. R., Johanning, L., & Smith, G. H. (2012). Assessing mechanical loading regimes and fatigue life of marine power cables in marine energy applications. *Proceedings of the Institution of Mechanical Engineers, Part O: Journal of Risk and Reliability*, *226*(1), 18–32. https://doi.org/10.1177/1748006X11413533

TML. Strain Gauges: Technical Specifications. E1007F. n.d. Accessed January 2, 2023. https://tml.jp/eng/documents/Catalog/Straingauges_E1007F.pdf.

Trim, A. D., Braaten, H., Lie, H., & Tognarelli, M. A. (2005). Experimental investigation of vortex-induced vibration of long marine risers. *Journal of Fluids and Structures*, *21*(3 SPEC. ISS.), 335–361. https://doi.org/10.1016/j.jfluidstructs.2005.07.014

Vandiver, J. K. (1993). Dimensionless Parameters Important to the Prediction of Vortex-Induced Vibration of Long, Flexible Cylinders in Ocean Currents. *Journal of Fluids and Structures*, *7*, 423–455.

Vandiver, J. K., Jaiswal, V., & Jhingran, V. (2009). Insights on vortex-induced, traveling waves on long risers. *Journal of Fluids and Structures*, *25*(4), 641–653. https://doi.org/10.1016/j.jfluidstructs.2008.11.005

Xu, W., Ma, Y., Ji, C., & Sun, C. (2018). Laboratory measurements of vortex-induced vibrations of a yawed flexible cylinder at different yaw angles. *Ocean Engineering*, *154*, 27–42. https://doi.org/10.1016/j.oceaneng.2018.01.113

Yin, D. (2022). Heave Motion Induced Vortex-Induced Vibrations of a Full-Scale Steel Lazy Wave Riser. *Journal of Offshore Mechanics and Arctic Engineering*, *144*(4). https://doi.org/10.1115/1.4054265

APPENDIX A

Strain gauges were connected in a full bridge Wheatstone configuration at each location, L1 to L7, spaced 0.5 m apart along the length of the cable (Figure A.1 (a)). At each location the total local bending strain was determined. Figure A.1 (b) depicts the arrangement of the strain gauges and their connection to the amplifier (V-link 200). Note that torsional effects may contribute to the curvature values, and these effects are not separated out in the current analysis. However, if pure bending strain values are used (from strain gauges aligned along the bending plane and assuming no off-axis effects), torsional effects should not directly influence the bending strain readings. Load cell analysis indicates that the torsional moment (M_z) is small but present, particularly when the current direction is inclined (e.g., 30°, 60°, 120°, 150°). The calculations for converting bending strain to curvature are as follows:

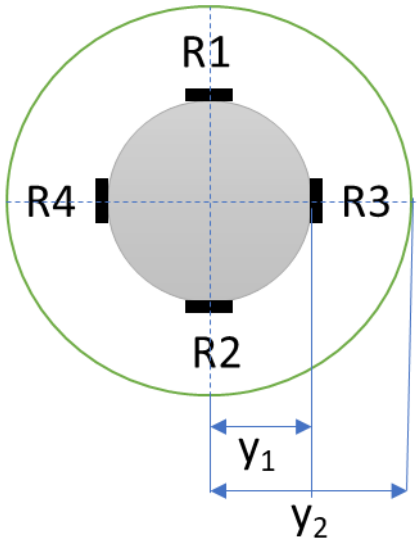

Figure A.1 Strain gauge locations around the inner cable

The strains at gauges 1 and 2 are given by $\frac{y_1}{\rho}$ and $-\frac{y_1}{\rho}$, where ρ is the radius of curvature and y_1 is the radius of the inner core cable (offset of the strain gauges from the neutral axis).

The resulting voltage difference, ΔV between junctions A and B is calculated as:

$$\Delta V = \frac{VKy_1}{2\rho} \tag{A.1}$$

where V is the excitation voltage and K is the gauge factor

The dimensionless curvature, κ is given by:

$$\kappa = \frac{y_2}{\rho} \tag{A.2}$$

Substituting the value for radius of curvature from Equation (A.1), we obtain

$$\kappa = 2\left(\frac{\Delta V}{V}\right)\frac{y_2}{y_1}\frac{1}{K} \tag{A.3}$$

where y_2 is the outer radius of the circle

The bending strain, ε_b, is related to the voltage by:

$$\varepsilon_b = \frac{1}{K}\frac{\Delta V}{V} \tag{A.4}$$

Substituting the value of ε_b from Equation (A.4) into Equation (A.3) gives

$$\kappa = 2\left(\frac{y_2}{y_1}\right)\varepsilon_b \tag{A.5}$$

For y_1 = 4.9 mm and y_2 = 15.5 mm, this simplifies to

$$\kappa = 6.33\varepsilon_b$$

Multiplying the bending strain, ε_b, by a factor of 6.33 yields the dimensionless curvature, κ, normalized by the outer radius of the cable.